Detection of Iron Protein Supercomplexes in *Pseudomonas aeruginosa* by Native Metalloproteomics

Mak A. Saito[1*] and Matthew R. McIlvin[1]
[1]Marine Chemistry and Geochemistry Department, Woods Hole Oceanographic Institution
Woods Hole MA 02543 USA

*Corresponding author: msaito@whoi.edu
Watson Biogeochemistry Building
360 Woods Hole Rd
Woods Hole MA 02543
USA

Running head: The Iron Metalloproteome of *Pseudomonas aeruginosa*

Abstract

Pseudomonas aeruginosa is a major contributor to infections in humans and is widely distributed in the environment. It is capable of aerobic and anaerobic growth, providing adaptability to environmental changes and in confronting immune responses. We applied high-throughput native 2-dimensional metalloproteomics to *P. aeruginosa* under oxic and anoxic conditions. Clear changes were observed in response to low O_2, including inducing the denitrification pathway and a variety of metal responsive proteins. The iron metalloproteome revealed four major iron peaks comprised of proteins with similar or synergistic functions: 1) respiratory and metabolic enzymes, 2) oxidative stress response enzymes, 3) DNA synthesis and nitrogen assimilation enzymes, and 4) denitrification enzymes and related copper enzymes. Three ferritins were observed in the metalloproteome and were coordinating with iron peaks 1 and 3. A number of metalloenzymes were more abundant at low oxygen, including: alkylhydroperoxide reductase C to deactivate organic radicals caused by denitrification, all three classes of ribonucleotide reductases, ferritin (increasing in ratio relative to bacterioferritin), and numerous denitrification enzymes. Superoxide dismutase and homogentisate 1,2-dioxygenase were more abundant at high oxygen. The four Fe peaks contained multiple iron metalloproteins of varying size, implying the presence cytosolic super protein complexes with related functions and dedicated iron storage. This also implies a cellular organization at the protein complex level optimized for metal trafficking and priotization. Together these results provide insight into the cytosol metallome and its response to oxygen and demonstrate the emerging capabilities of metalloproteomic methods in understanding metal use and protein-protein interactions in biological systems.

Graphical Abstract

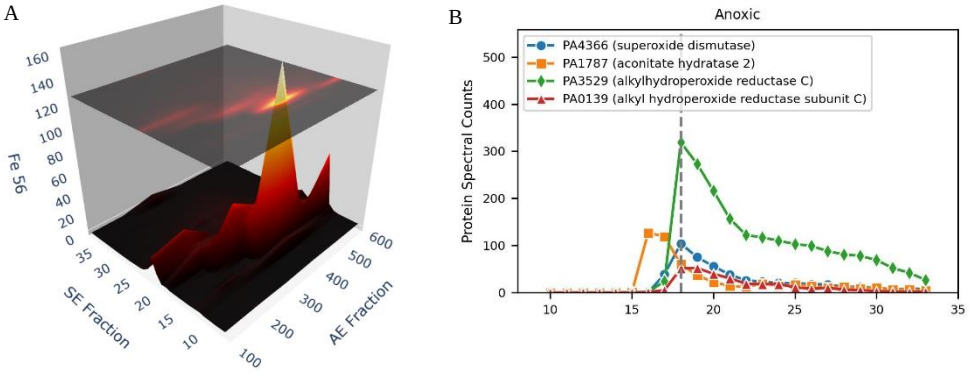

The iron metalloproteome of *Pseudomonas aeruginosa* was examined using native (non-denaturing) 2-dimensional chromatographic separation coupled to elemental and proteomic mass spectrometries. Four major iron peaks were observed that corresponded to multi-protein complexes associated with respiratory, antioxidant, DNA production, and denitrification functions, and associated iron storage and supply. The results demonstrate the complex adaptations this microbe has regarding iron homeostasis and trafficking.

Introduction

The pseudomonad bacterium are a group of widely distributed microbes found in both the environment and as pathogens[1,2]. The species *Pseudomonas aeruginosa* is a major contributor to infections in humans including in wounds and lungs of cystic fibrosis patients, as well as the cause of nosocomial infections such as pneumonia and septicemia[3]. Due to the prevalence of *P. aeruginosa* infections and increasing occurrence of antimicrobial resistance, the World Health Organization has classified it as a priority pathogen and recommended development of new antimicrobial strategies[4]. Furthermore, the role of metals is important in nutritional immunity, for example where immune cells are also targeting the availability of metals[5]. In the environment *P. aeruginosa* can be found in soils and aquatic environments, such as sediments and sinking particles, as part of the microbial community that is decomposing organic matter[6–8].

Pseudomonas is capable of rapid growth, consistent with a copiotrophic lifestyle that allows it to proliferate quickly. Moreover, Pseudomonads are capable of multiple respiratory pathways that allows them to continue growth under suboxic or anoxic conditions, such as by growth on the oxidant nitrate via denitrification[9,10]. When infecting host tissues, *Pseudomonas aeruginosa's* oxygen flexibility is advantageous, where it resists neutrophil cells' oxidative bursts through the use of multiple superoxide dismutases, as well as also actively consuming oxygen to reducing the effectiveness of those neutrophils[11]. *Pseudomonas* has a relatively large genome for a bacterium, with over 5000 genes in the core genome[12], and 5570 genes in the genome of PAO1[13], reflecting these dynamic capabilities. Adaptations to acquire sufficient metal nutrition is known to be an important trait of *Pseudomonas aeruginosa,* and *P. aeruginosa* use of iron is particularly complex with regard to acquisition and homeostasis capabilities. As a result, an active area of development for antimicrobials involves drugs that target iron acquisition or trafficking, such antibiotic conjugated to siderophores, or inhibitors for iron release from ferritin. Amongst *P. aeruginosa*'s sophisticated iron capabilities are the biosynthesis capability for two siderophores, pyoverdine and pyochelin, which are fluorescent and give cultures a characteristic visible coloration. *P. aeruginosa* also acquires iron through exogenous siderophores, through a ferrous iron transporter, and when complexed to heme, citrate, and catechols[14]. Metal insufficiencies caused through mutation of transporter systems often result in decreased pathogenicity, demonstrating the importance of metal nutrition in *P. aeruginosa* infections[15], as well as the potential avenues for antibiotic treatment by inhibiting transporters or complexing by exogenous metallophores[14,16].

With this array of metal uses within *P. aeruginosa*, understanding the composition and variability of this microbe's metallome is of broad interest. The study of metalloproteins typically focuses on the characterization of individual enzymes or proteins to provide key mechanistic insights. Cellular metallome studies often focus on the overall metal cellular content by bulk metal analyses, or by localization of metals intracellularly with imaging approaches. Metalloproteomic techniques can complement these approaches by reconstructing the contribution of the composite of metalloenzymes and metalloproteins to the overall metallome. This approach combines native extraction of metalloproteins and their detection by dual mass spectrometry analyses to determine both metal and protein content simultaneously to assess major metalloproteins inventories within an organism[17–20]. In this study we conducted a metalloproteomic analysis of *P. aeruginosa* grown under aerobic and anaerobic conditions to assess how the iron metalloprotein inventory changes in response to these environmental conditions. A follow-up study will present the results of additional metals in the *P. aeruginosa* metalloproteome.

Methods

Isolation and Cultivation: Microbiological plates for isolation were made with marine broth media (Zobell's media) with prepared from 500 mL of 0.2 µm-filtered coastal seawater (Vineyard Sound) with the addition of 2.5 g peptone (Fisher Scientific) and 0.5 g yeast extract (BD Difco), with 7.5 g of agar, followed by autoclaving for 40 min. For cultivation marine broth media (Zobell's media) with prepared by autoclaving of 500 mL of 0.2 µm-filtered coastal seawater (Vineyard Sound) with the addition of 2.5 g peptone (Fisher Scientific) and 0.5 g yeast extract (BD Difco). Plates were streaked with inoculum from on the METZYME expedition (KM1128) from the 51 micron filter from filter pump 2 collected at 400m at Station 5 (0°S 202°E) on October 13 2011 in the Central Pacific Ocean on the R/V Kilo Moana and allowed to incubate at room temperature. Picked colonies from plates grown in liquid media displayed coloration characteristic of *Pseudomonas aeruginosa*. Once colonies had grown, a colony was restreaked and frozen into, streaked again and frozen -80 in glycerol and shipped to the laboratory. Experiments were conducted with strain 2-54. While *P. aeruginosa* is known to be found in natural environments, including coastal environments, it is not often observed in open ocean (oceanic) environments. The sampling location was oceanic, although there were islands present in the broad geographic vicinity (Hawaii and Christmas Island of Kiribati). While this was an attempted isolation from the natural ocean environment, given genomic results (see below), the lack of *Pseudomonas aeruginosa* observed in co-occurring metagenomes and metaproteomes datasets[21,22], we infer that this isolate was a contaminant either from the laboratory or ship during the isolation process.

Genomic analyses: A bacterial isolate was genomic sequenced was sequenced at the Johns Hopkins Deep Sequencing and Microarray Core Facility using Oxford Nanopore and assembled using Canu, Nanopolish, and circulator pipeline. BLAST analyses and resulting annotations determined the microbe to be *Pseudomonas aeruginosa*.

Genome Database for Proteomics Analysis: Given the minor differences between PAO1 and our isolate, and the high-quality annotations associated with PAO1, the PAO1 genome was used for proteome annotation. PAO1 was downloaded from NCBI in January of 2019, allowing use of the well-established PA identification numbers.

Anoxic Media: Anoxic media (anaerobic) treatments were conducted by autoclaving 1L bottles of media into followed by cooling, 8.8e-4M of sterile-filtered sodium nitrate was added as an alternate oxidant to oxygen and to enable denitrification, then the media was equilibrated with a loose cap in an anerobic glove box for several days to allow equilibration to the no oxygen environment. Anoxic bottles were then inoculated in the glove box, closed tightly, and vacuum heat sealed within a plastic bag. Oxic cultures were allowed to grow with a loose cap and moderate shaking to allow gas exchange. Cells were grown in an incubator at 37°C with continuous moderate mixing. Culture aliquots were harvested by centrifugation at 3220 × *g* for 40 min at 4 °C using an Eppendorf 5810R centrifuge and 50mL centrifuge tubes, decanted and pellets were frozen until analysis. 50mL aliquots of each treatment were extracted for metalloproteomics to survey metalloprotein inventories and accompanying global proteomics to verify metabolic responses to environmental oxygen.

Protein analyses

Protein extraction: Pellets were resuspended in 5ml of protein extraction buffer (50mM HEPES pH 8.5 (Boston BioProducts #BB-2082), 1% SDS in HPLC grade water). All reagents in this protocol are made with HPLC grade water. Samples were heated at 95˚C for 10 minutes and shaken at room temperature

for 30 minutes. Samples were then spun for 30 minutes at 3220 x *g* in an Eppendorf 5810 centrifuge. Supernatant was removed from pellet and transferred to a Vivaspin 5K MWCO ultrafiltration unit (Sartorius Stedim #VS0611). Protein extract was concentrated to approximately 350 µL, washed with 1ml of lysis buffer and transferred to a 2ml ETOH washed microtube (all tubes from this point on are ETOH washed). Vivaspins were rinsed with small volumes of protein extraction buffer to remove all concentrated protein and all samples were brought up to 400µl.

Protein quantification: Standard curves were generated using albumin standard (Thermo Scientific #23210). Total protein was quantified after extraction and after purification with 2µl of sample in duplicate using the BCA method (Thermo Scientific Micro BCA Protein Assay Kit #23235). Absorbance was measured on a Nanodrop ND-1000 spectrophotometer (Thermo Scientific).

Protein reduction and alkylation. 50 units (2 µl) of benzonase nuclease (Novagen #70746-3) was added to each sample and incubated at 37˚C for 30 minutes. Samples were reduced by adding 20 µl of 200 mM DTT (Fisher #BP172-5) in 50mM HEPES pH 8.5 at 45˚C for 30 minutes. Samples were alkylated by adding 40 µl of 400mM iodoacetamide (Acros #122270050) in HEPES pH 8.5 for 30 minutes at 24˚C, occasionally heating to 37˚C to prevent precipitation. The reaction was quenched by adding 40 µl of 200 mM DTT in 50mM HEPES pH 8.5.

Protein clean up and digestion. SpeedBead Magnetic Carboxylate Modified Particles (GE Healthcare #65152105050250 and #45152105050250) were prepared according to Hughes et al. (2014). 20 µl (20 µg/µl) of magnetic beads were added to 400 µl of extracted protein sample. Samples were heated at 37˚C periodically to avoid precipitation. Samples were acidified to a pH of 2-3 by adding 50 µl of 10% formic acid. 2X volume (1100 µl) of acetonitrile was immediately added. Samples were incubated at 37˚C for 15 minutes and then at room temperature for 30 minutes. Samples were placed on a magnetic rack, incubated for 2 minutes, supernatant was removed and discarded. Samples were washed 2 times removing and discarding supernatants with 1400 µl of 70% ETOH for 30 seconds on the magnetic rack. 1400 µl of acetonitrile was added to each sample for 30 seconds on the magnetic rack. Supernatant was removed and discarded. Samples air dried for approximately 4 minutes until acetonitrile had just evaporated. Samples were removed from the magnetic rack and beads were reconstituted in 90 µl of 50 mM HEPES pH 8.0. Purified protein was quantified as described above. Trypsin (Promega #V5280) dissolved in HEPES pH 8.0 at a concentration of 0.5 µg/µl was added to samples at a 1:25 trypsin to protein ratio and incubated at 37˚C overnight.

Peptide recovery and preparation. Acetonitrile was added to digested peptides at a concentration of ≥ 95% and incubated for 20 minutes at room temperature. Samples were then placed on the magnetic rack for 2 minutes and the supernatant was removed and discarded. 1400 µl of acetonitrile was added to samples on the magnetic rack for 15 seconds. Supernatant was removed and discarded. The sample were air dried for approximately 4 minutes, just until acetonitrile was evaporated. Beads were reconstituted in 90 µl of 2% DMSO and incubated off the rack at room temperature for ≥ 15 minutes. Samples were centrifuged slowly and briefly at 900 rcf to remove liquid from the tube walls. Samples were incubated on the magnetic rack for 15 minutes and supernatant containing peptides was transferred to a new ETOH washed 1.5 ml microtube. This step was repeated to ensure removal of all magnetic beads. 1% trifluoroacetic acid was added to samples for a final concentration of 0.1%. Samples were zip tipped with Pierce C18 tips (Fisher #87784) according to manufacturer's protocol with a final resuspension in 25 µL of 70% acetonitrile, 0.1% formic acid. Samples were evaporated to approximately 10 µl in a DNA110 Speedvac (ThermoSavant). Samples were finally resuspended to a peptide concentration of 1 µg/µl in buffer B (2% acetonitrile, 01% formic acid).

Peptide analysis. Protein extracts were analyzed by liquid chromatography-mass spectrometry (LC-MS) (Michrom Advance HPLC coupled to a Thermo Scientific Fusion Orbitrap mass spectrometer with a Thermo Flex source). 1 µg of each sample (measured before trypsin digestion) was concentrated onto a trap column (0.2 x 10 mm ID, 5 µm particle size, 120 Å pore size, C18 Reprosil-Gold, Dr. Maisch GmbH) and rinsed with 100 µL 0.1% formic acid, 2% acetonitrile (ACN), 97.9% water before gradient elution through a reverse phase C18 column (0.1 x 250 mm ID, 3 µm particle size, 120 Å pore size, C18 Reprosil-Gold, Dr. Maisch GmbH) at a flow rate of 500 nL/min. The chromatography consisted of a nonlinear 160 min gradient from 5% to 95% buffer B, where A was 0.1% formic acid in water and B was 0.1% formic acid in ACN (all solvents were Fisher Optima grade). The mass spectrometer was set to perform MS scans on the orbitrap (240000 resolution at 200 m/z) with a scan range of 380 m/z to 1580 m/z. MS/MS was performed on the ion trap using data-dependent settings (top speed, dynamic exclusion 15 seconds, excluding unassigned and singly charged ions, precursor mass tolerance of ±3ppm, with a maximum injection time of 150 ms). Mass spectra were searched against Pseudomonas aeruginosa PA01 proteome using Proteome Discoverer 2.0 using the SEQUEST HT algorithm (Thermo) with a parent tolerance of 10 ppm and a fragment tolerance of 0.6 Da. Proteome Discoverer output files were then loaded in Scaffold (Proteome Software) with a protein threshold maximum of 1.0% false discovery rate.

Metalloproteomic Methods

Protein Separation. Cell pellets from 50 mL centrifuge tubes were thawed in an anaerobic chamber (Coy Laboratory Products Inc.) and suspended in 5 mL of 50 mM TRIS buffer (pH 8.8, all buffers Chelex treated to remove background metals). The solution was transferred to a 15 mL PET plastic centrifuge tube (Fisher 055391) before sonication on ice for 2 minutes (1 second on/off pulses with a 5 min stop after 1 min, Fisherbrand Model 120 sonic dismembrator). The sonicated pellet was diluted to a total volume of 30 mL in two 15 mL tubes and centrifuged in a gas tight bucket rotor for 60 min at 3220 × g at 5 °C (Eppendorf 5810R). The supernatant was loaded onto a GE HiTrap Q HP anion exchange column with a peristaltic pump at 0.25 mL/min. The column was then attached to an Agilent 1100 series HPLC pump and eluted with a gradient of sodium chloride at 0.5 mL/min, where buffer A was 50 mM TRIS buffer (pH 8.8), and buffer B was 1 M NaCl in 50 mM TRIS buffer (pH 8.8). The gradient was 2 min at buffer A, followed by a linear increase to 60% buffer B over 12 min, then another linear increase to 100% buffer B over 6 min. Eluent was collected with a Bio-Rad 2110 fraction collector in 2 mL microcentrifuge tubes at a rate of 1 fraction every 2 min and stored on ice. Anion exchange column fractions were concentrated using 5000 Da molecular weight cutoff Vivaspin columns from 500 µL to 100 µL before size exclusion separation. Concentrated samples were injected into a Tosoh Bioscience TSKgel G3000SWxl size exclusion column with guard column attached to a Michrom Paradigm MS4 LC system with a CTC Analytics HTC Pal autosampler, and samples were eluted with a 0.5 mL/min isocratic gradient of 50 mM Tris buffer (pH 7.5, 50 mM sodium chloride). Fractions were collected in 1 min intervals into 1.2 mL 96 well plates. 250 µL of each well was transferred to another 96 well plate for metals analysis.

Protein analysis of metalloproteins. 200 µL of each sample was combined with 10 µL acetonitrile and 15 µL of 10 mM dithiothreitol in 100 mM ammonium bicarbonate. The samples were incubated for 30 min at 70 °C while shaking at 450 rpm. After cooling to room temperature, 30 µL of 20 mM iodoacetamide in 100 mM ammonium bicarbonate was added to each well and incubated for 30 min in the dark. 10 µL of 0.03 µg/µL trypsin (Promega Gold) was added to each well and incubated overnight at 37 °C while shaking at 450 rpm.

Trypsin digested size fractionated samples were analyzed using a Michrom Advance HPLC system with reverse phase chromatography coupled to a Thermo Scientific Q-Exactive Orbitrap mass spectrometer with a Michrom Advance CaptiveSpray source. Each sample was concentrated onto a trap column (0.2 x 10 mm ID, 5 µm particle size, 120 Å pore size, C18 Reprosil-Gold, Dr. Maisch GmbH) and rinsed with 100 µL 0.1% formic acid, 2% acetonitrile (ACN), 97.9% water before gradient elution through a reverse phase C18 column (0.1 x 150 mm ID, 3 µm particle size, 120 Å pore size, C18 Reprosil-Gold, Dr. Maisch GmbH) at a flow rate of 500 nL/min. The chromatography consisted of a nonlinear 50 min gradient from 5% to 95% buffer B, where A was 0.1% formic acid in water and B was 0.1% formic acid in ACN (all solvents were Fisher Optima grade). The mass spectrometer monitored MS1 scans from 380 m/z to 1580 m/z at 70K resolution. MS2 scans were performed at 15K resolution on the top 10 ions with an isolation window of 2.0 m/z and a 10 second exclusion time.

Metals analysis of metalloproteins. 250 µL of each size fractionated sample was combined with 50 µL of 30% hydrogen peroxide (MilliporeSigma Supelco, trace metal grade) and digested overnight. 500 µL of 5% nitric acid containing 1 ppb Indium was then added and digested overnight. Samples were analyzed on an ICAP-Q inductively coupled plasma-mass spectrometer (Thermo) with an SC-4 DX FAST autosampler (Elemental Scientific, Inc.). Samples were analyzed in KED mode with helium as the collision gas. The following metal isotopes were analyzed: Fe 56, P 31, Co 59, Zn 66, Ni60, Cu63, Al27, Ti48, V51, Cr52, Mn55, Fe57, As75, and Mo95. Metals were calibrated to standard curves prepared the same as the samples (96 well plates, identical reagents) and run between each set of anion exchange fractions. Metal blanks were subtracted by taking the average of the final AE and last five SEC fractions (AE8, SEC 34-38). These end values were slightly lower than the initial values and likely reflected more instrument conditioning.

Comparability between Oxic and Anoxic Metalloproteomes: Efforts were made to make the results between oxic and anoxic metalloproteomes consistent to allow comparisons. The total protein yields from the 1st dimension were measured by total protein assay (see above) (Figure S1). This was the protein material loaded into the 2nd SE dimension. The total protein was relatively similar between oxic and anoxic treatments, ranging between 9 and 56% more in the anoxic treatment in all cases, and the smallest difference occurring at the peak protein fraction for both (300-400mM; Table S1 and Figure S1).

Data analysis

The metals and protein datasets had slightly different ranges of data coverage, as summarized in Table S1. The 2D data was visualized in 6-8 anion exchange (AE) fractions as the first dimension (100-200mM, 200-300mM, 300-400mM, 400-500mM, 500-600mM, 600-800mM, 800-1000mM, 1000-1000mM, where the last two ranges were only available in the oxic metals dataset) and 38 size exclusion (SEC) fractions in the second dimension for a grid of 304 samples. AE values were plotted as the lower value of their AE ranges (100, 200, 300, 400, 500, 600, 800, 1000). Metals and proteins were analyzed from a subset of SEC fractions, 7-38 for metals and 10-35 for proteins. Two initial AE fractions containing largely dead volume (0 and 0-100mM) were not analyzed for metals or proteins.

Informatics methods

Four dataframes, oxic and anoxic metals and proteins, were prepared in Excel and imported into a Jupyter notebook (Version 7.2.2) using customized Python code (Version 3.10.9 Anaconda package) to create visualization, identify maxima, and conduct optimization fitting. Visualizations were made using Matplotlib and Plotly packages. The code is available at GitHub at https://github.com/maksaito/Metalloproteomic-Viewer (Version 11). The workflow consisted of identifying major metal peaks, identifying the proteins with maxima on or adjacent to the metal peak,

identifying metalloproteins within the list using Copilot AI, calculating the contributions of proteins to the iron peak in the SE dimension using the Broyden, Fletcher, Goldfarb, and Shannon local search optimization algorithm (L-BFGS-B optimization routine and minimize function in Python). Protein structures and putative protein-protein interactions were created using Alphafold3.[23]

Results and Discussion

Global Proteomics

Cultures grown under aerobic and anoxic conditions were screened using proteomics to verify acclimation to each treatment prior to metalloproteome analyses. Proteomic results clearly showed acclimation to the presence or absence of oxygen, these results are summarized here, and a more complete proteomic analysis of oxygen variation will be presented in a future study. Briefly, selected proteins showed clear changes in protein abundance in response to O_2, including the denitrification pathway (nitrate, nitrite, nitrous, nitric oxide reductases), which contain numerous metalloenzymes involving Fe, Cu and other metals (Figure 1). A number of other metal-related proteins also were more abundant under anoxic conditions including molybdopterin biosynthesis proteins, cobalt chelatase CobN from cobalamin biosynthesis pathway[24], and the CopR copper regulator[25]. Anaerobic molybdopterin biosynthesis is consistent with Mo use within nitrate reductase.

As a component of the B_{12} biosynthetic pathway, the increased abundance of cobalt chelatase CobN under anoxic conditions contrasted with a prior model that proposed aerobic B_{12} production, secretion and diffusion into anaerobic layers, and uptake. Because *P. aeruginosa* only has the oxygen-requiring enzymes for cobalt insertion in B_{12} biosynthesis (CobNST; as opposed to the oxygen independent cbiK/X found in other microbes), Crespo et al. proposed a model where B_{12} is produced aerobically in the upper biofilm layer, then must be secreted and diffuse to inner anaerobic layers where it is used for NrdJ; and once depleted the Fe RNR-III (NrdD) is used below[26]. Ribonucleotide reductase enzymes also showed large changes in protein abundance between aerobic and anaerobic conditions (Figure 1; also see Fe Peak 3 section)[26]. Under aerobic conditions Class I NrdAB proteins were most abundant, with less of the class II NrdJab, and no observed class III NrdD. Under anaerobic conditions all three classes of RNR's were present and in higher abundance than in oxic treatments. Similar to CobN, these results also contrast with the prior model, where a cascade of expression from NrdA to NrdJ to NrdG was expected to coincide with decreasing B_{12} availability. Our experiments were conducted with mild shaking, thereby discouraging biofilm formation which may contribute to the differences with the prior study.

Overall the results global proteomic survey demonstrated clear differences between oxic and anoxic treatments, particularly with regards to the denitrification apparatus. As a result, metalloproteomic analyses were conducted to determine changes in the metallome under oxic and anoxic conditions.

Metalloproteomics Overview

Metalloproteomic analyses were conducted on sample splits from the oxic and anoxic treatments from the global proteomic results. This study focuses primarily on the iron metalloproteome, with the additional contextual Cu data. A future study will examine additional metals.

The *P. aeruginosa* iron metalloproteome had four major peaks in the native 2-dimensional space if anion exchange (AE) and size exclusion (SE), labeled Fe Peaks 1-4 hereon (Figures 2 and 3, Figure S2, Table 1). Notably the protein content of these Fe peaks was associated with major cellular functions, with Fe Peak 1 containing the oxic respiratory system and the bulk of iron storage. Fe Peak 2 was close in proximity to Fe Peak 1 and contained antioxidant functions. Fe Peak 3 was located higher in the AE dimension and contained the two iron forms of ribonucleotide reductase. Finally, Fe Peak 4 was found at

the low end of the AE dimension and contained proteins associated with the denitrification capabilities. Notably Fe Peaks 3 and 4 showed increased Fe and protein content under the anoxic condition. The following sections describe the contents of the four major iron peaks, followed by a section about iron storage capabilities. A list of metalloproteins within each Fe Peak is provided in Table S2.

While the metalloproteomic methodology was developed with the intention of maintaining the native metal-protein relationship, the results presented here also support notion that the native extraction methodology preserve some multi-protein complexes (MPCs). As a result, the co-elution of multiple iron (and other) proteins within the four iron peaks described below may be neither coincidental nor due to limited chromatographic resolution, but remnants of *in vivo* protein-protein interactions. The final section of this manuscript briefly discusses this potential useful aspect of the metalloproteomic method.

Fe Peak 1

The largest peak (Fe Peak 1) was located at AE-SE location 400-14 in oxic conditions and 400-15 in anoxic conditions (Figure 2). Five iron proteins co-eluted within this region (Figure 4), aconitase (annotated as aconitate hydratase 2 PA1787), homogentisate 1,2-dioxygenase (HmgA, PA2009), and hydrazone dehydrogenase (HdhA, PA4022), two ferritins (annotated as bacterial ferritin PA4235 and bacterioferritin PA3531).

Fe Peak 1a: Aconitase was the most abundant iron protein with a large and very broad peak in both oxic and anoxic datasets that extended through multiple anion exchange fractions (AE 300-500 along SE 16 in oxic and AE 300-600 along SE 16-17; Figures 3C, 3D, 4A, 4B), reaching 173 and 228 spectral counts at each AE 400 maxima, respectively. However, both aconitase maxima were offset from the Fe Peak 1 maxima (along AE 400): under oxic conditions aconitase was at SE 16 versus Fe Peak 1 at SE 14, while under anoxic conditions aconitase was at SE 17 versus Fe Peak 1 at SE 15. There is a shoulder in Fe Peak 1 towards higher SE fractions, and the aconitase offset likely contributes to this. Moreover, in the metalloproteome of the marine bacterium *Pseudoalteromonas*, a similar offset of aconitase was observed, where a second peak was offset from one that aligned with iron, and was interpreted as a potential apo form[19]. Given the breadth of aconitase in the *P. aeruginosa* metalloproteome, it also seems feasible that the metalated form occurs at the lower SE range, alsowhere the bacterioferritin and ferritin co-eluted (Figure 4C and 4D). Moreover, the breadth might also reflect the extent of protein-protein interactions and resulting MPCs, where ferritin proteins can provide the source of iron to aconitase and other metalloproteins in Fe Peak 1.

Fe Peak 1b: Another enzyme within Fe Peak 1, homogentisate 1,2-dioxygenase (PA2009, HmgA), was over 11-fold more abundant in the oxic treatment relative to the anoxic treatment (maximum of 67 and 6 spectral counts, respectively). This enzyme is involved in the degradation of aromatic rings including tyrosine and phenylalanine to produce the metabolite homogentisate (2,5-dihydroxyphenylacetate, HG), and requires oxygen for activity. It is a homo-6mer with an iron cupin site, where the cupin β-strands have a characteristic metal binding motif[27]. HmgA was observed to be one of the few genes downregulated in the hypervirulent Australian *P. aeruginosa* clinical strain AES-1 under chronic infection cystic fibrosis patients, relative to acute infection systems, and hence was characterized as an important component of *P. aeruginosa's* adaptation to the cystic fibrosis lung environment[28]. HmgA is also important in humans: a mutation to HmgA causes the rare genetic disease alkaptonuria, which causes an accumulation of homogentisic acid, due to the inability to break down tyrosine and phenylalanine, which polymerizes inside the body and as a dark pigmentation and causing severe arthropathy[29]. Its abundance and responsiveness to oxygen within the largest iron peak in this study is consistent with these prior studies and suggests that if HmgA AES-1 responds similarly to oxygen, the cystic fibrosis lung microbiome environment experiences hypoxia conditions.[30]

Fe Peak 1c: The iron enzyme hydrazone dehydrogenase HdhA (PA4022) also co-eluted with Peak 1, and transitions from being a minor peak in the oxic conditions to a major peak that also aligns with the iron maxima in the anoxic conditions. HdhA transforms hydrazones, molecules with a C=N-N moiety, to hydrazides and acids. Prior studies observed that PAO1 grown on hydrazone adipic acid bis(ethylidene hydrazide) as a carbon source upregulated *hdhA*, and mutants of the gene negatively affected growth rate in the same media[31]. Fe Peak 1 was four times larger in anoxic conditions compared to oxic conditions, despite only having 9% more total protein (Table S1). The alignment of HdhA with Fe peak 1 and HdhA's increased abundance under anoxic conditions implies it contributes to the larger anoxic Fe Peak 1.

Comparing this with the prior HmgA, both proteins co-eluted at Fe Peak 1, but one protein was more abundant under oxic conditions (HmgA)and the other under anoxic conditions (HdhA), implying a shifting influence of proteins contributing to Fe Peak 1 with the change in oxygen availability.

Fe Peak 1d: The Fe metalloprotein catalase (PA0236) also eluted within Fe Peak 1 in both oxic and anoxic conditions. This enzyme is responsible for the deactivation of hydrogen peroxide. With aconitase being highly sensitive to reactive oxygen species which cause degradation of its iron-sulfur clusters[32], the close proximity of these two enzymes is beneficial.

Fe Peaks 1e and 1f: Two ferritin iron storage proteins contributed to Fe Peak 1, and a comprehensive discussion of ferritins in the *P. aeruginosa* metalloproteome will be discussed in a later section.

Optimization of contributions to Fe Peak 1: quantitative reconstruction of Fe Peak 1 was conducted using optimization approach along the AE 400 1st dimension for both oxic and anoxic conditions (Figure 5). The double peak of PA2009, where the second peak may have been apo based on lack of iron detected there, results in it being penalized in the optimization. When the second PA2009 peak was manually adjusted to have zero spectral counts, it became a significant component to Fe Peak 1 (Figure S3).

Fe Peak 2

The second largest iron peak within *Pseudomonas* was at 300-17 under oxic conditions and 300-18 (Figure 2). This peak is adjacent to the Peak 1 described above and hence shares some protein overlap of protein features. Several iron proteins have maxima associated with Peak 2: the iron superoxide dismutase (SodB, PA4366), two copies of alkylhydroperoxide reductase C (PA3529 and PA0139) and quinone oxidoreductase (PA0023; Figure 6). Within the oxic Fe peak there is a shoulder towards the lower SE fractions, caused by a second peak at 300-15 that is likely associated with the aconitate hydratase 2 protein (PA1787; Fe Peak 1a) and its broad elution pattern mentioned above that continues at 300-16 (Figure 2, Figure 3A, 3E) that contributed to both the AE 300 and AE 400 dimensions.

Fe Peak 2a: In *P. aeruginosa*, FeSOD (SodB, PA4366) has been reported to be produced constitutively, including under anaerobic conditions, while the MnSOD (SodA, PA 4468) is only produced under oxic stationary phase conditions[33,34]. These SODs, with catalase, contribute to defense against oxidative bursts from host neutrophil cells[11]. Our results are consistent with these prior findings, where the MnSOD was not identified in the oxic or anoxic metalloproteomes which were both harvested in exponential growth, and the FeSOD was abundant in both treatments. Moreover, the Mn maximum was not aligned with the FeSOD implying no substitution in this SOD isoform (Figure 6G and 6H).

Fe Peak 2b and 2c: The two copies of alkylhydroperoxide reductase C (AhpC; PA3529 and PA0139) also co-elute in the 2nd largest iron peak (Figures 6A and 6B). These sequences were checked using METATRYP software and do not share any tryptic peptides, meaning their proteomic results are independent of each other[35]. AhpC contributes to the cell's antioxidant capability by removing organic peroxides such as peroxynitrite and is part of the 2-Cys peroxiredoxin family. As a result AhpC has been

described as "the most widely distributed [reactive nitrogen intermediate (RNI)] resistance gene known"[36]. AhpC is also the primary scavenger of hydrogen peroxide in *E. coli*, where catalase mutants rely on this enzyme for anti-peroxide activity[37]. Hare et al.[38] observed the PA3529 alkylhydroperoxide reductase C to have increased abundance expressed under peroxide stress treatments in *P. aeruginosa* strain PAO1, in addition to superoxide dismutase and catalase. PA3529 immediately precedes bacterioferritin-associated ferredoxin Bfd (PA3530) and bacterioferritin (PA353) in the genome, implying co-regulation of this gene neighborhood. AhpC also exhibits chaperone activity, preventing misfolding and thermal aggregation of proteins[39]. This dual function of AhpC is thought to convey its adaptability to oxidative and environmental stresses[39]. AhpC exists as either a dimer or a decamer in physiological solutions.

Notably, both AhpC proteins are present in the metalloproteome contributing to Fe Peak 2, with PA3529 having higher spectral counts than PA0139 in both oxic and anoxic conditions (Figure 6A, 6B). One notable difference between conditions is that PA3529 goes from being the 3rd most abundant iron protein in Fe Peak 2 after superoxide dismutase and aconitase under oxic conditions (where it was tied with aconitase at the iron maximum with 96 spectral counts), to the primary iron protein under anoxic conditions at 319 spectral counts. The minor AhpC (PA0139) also increased under anoxic conditions from 33 to 52 spectral counts. Both AhpC proteins were quite minor constituents to Fe Peak 1, with under 18 or fewer spectral counts for oxic conditions, and 9 or less spectral counts for anoxic conditions offset from the peak 1 maximum (centered between SE 11-13 in both cases). Given the switch to nitrate-based respiration in the anoxic treatment, the increased abundances of both AhpC's and their contribution to the overall metallome was likely due to the increased production of organic peroxides like peroxynitrite, and the need to deactivate them to prevent toxicity. Given the prevalence of hypoxic conditions within *P. aeruginosa* infections and its increased abundances, inhibitors to the AhpC could be a potential antimicrobial therapeutic target[36].

Fe Peak 2d: Quinone oxidoreductase is an antioxidant enzyme catalyzes the reduction of quinones preventing the formation of semiquinones that generate reactive oxygen species.[40] In bacteria the enzyme plays a critical role in the electron transport chain, catalyzing the transfer of electrons from NADH to quinone, and contains multiple iron-sulfur clusters[41]. Interestingly, NAD(P)H quinone oxidoreductase is often highly expressed in cancers, and hence is considered a drug target[42].

Fe Peak 3

The third largest iron peak in the *P. aeruginosa* metalloproteome occurred in the 1st dimension AE 600 mM and AE 500mM fractions. Here we consider oxic peak AE 600-SE 18, and anoxic peak AE 600-SE 14 both as Fe Peak 3 given their relative proximity in the iron visualizations and some shared proteins (Table 1, Figures 2, 3, 7A-F; note Figure 2 has expanded AE range to AE 1000 which includes Fe Peak 3). Notably the anoxic Fe peak 3 was 5-fold larger than the oxic peak in the AE 600 dimension. The total protein in the anoxic 600mM AE fraction was only 23.1% larger than the oxic, not enough to account for the 5-fold Fe difference, hence we interpret this as a biological signal. There was a divot in many protein abundances at anoxic Fe enzymes at AE600-SE14 (Figure 7D) where the iron maxima occurred. This appears to be related to an instrument or sample processing issue, where the overall signal for that protein sample was 1/10th that of the surrounding samples (Figure 7B). Because of this divot, we also examined for overlap of proteins and iron with the adjacent AE 500 dimension, where there was an Fe peak at SE 15 for both, relatively close to the anoxic AE600-SE14, and a bit more removed from the oxic AE600-SE18. As a result, AE 500mM is included in the Fe Peak 3 discussion here (Figure 7G-J, Table S1).

Proteins in oxic treatment: At oxic AE 600-18 there were no proteins with maxima that co-elute at that precise location. Of all 33 proteins identified at that location, only three were known iron proteins (Figure 7A, C, E): glutamine synthase (PA5119), aconitate hydratase 2 (PA1787), and L-cysteine desulfurase (pyridoxal phosphate-dependent, PA3814).

Proteins in anoxic treatment: At anoxic 600-14, there were also no proteins with maxima at this precise location. Of the 59 proteins detected at that location, the three iron proteins found in oxic AE 600-18 were present here, as well as additional the potential iron proteins (Figure 7B, E, F): aconitate hydratase 1 (PA1562), nitrite reductase precursor (PA0519), electron transfer flavoprotein alpha-subunit (PA2951), DNA-binding protein from starved cells, Dps (PA0962), and ferric uptake regulation protein (PA4764), NrdA, catalytic component of class Ia ribonucleotide reductase (PA1156) and NrdB, tyrosyl radical-harboring component of class Ia ribonucleotide reductase (PA1155), class III (anaerobic) ribonucleoside-triphosphate reductase subunit, NrdD (PA 1920). There were 8 unannotated proteins that eluted with maxima at 600-18 under anoxic conditions (PA3309, PA2765, PA0916, PA2817, PA3982, PA2151, PA3850, PA0457). Together these oxic and anoxic proteins are listed as Fe Peak 3a-k (Table S2), and selected proteins are discussed here.

Fe Peak 3a: Glutamine synthetase was the most abundant enzyme in both oxic and anoxic treatments on the Fe Peak 3 (along the AE600 dimension, Figure 7A and B), yet its peak was shifted larger in the size exclusion spectrum at SE 13 in both treatments, implying that perhaps the apo form may have been associated with a larger protein complex. This enzyme is important in nitrogen metabolism that converts glutamate and ammonia into glutamine[43].

Fe Peak 3b and 3c: The ribonucleotide reductase subunits NrdAB were the next most abundant iron metalloproteins in the anoxic AE500 and AE 600 dimensions (Figure 7C, H), and the AE 500, but the AE 600 dimensions of the oxic treatment (Figure 7C, G). The ribonucleotide reductases are a key enzyme in DNA replication by providing the necessary dNTP substrates. *P. aeruginosa* is unusual in that it contains all three classes of ribonucleotide reductases within their genomes (RNR I-III)[44,45]. Most RNRs are metalloenzymes, with RNR-I (NrdAB) subclasses having Fe-Fe, Fe-Mn, Mn-Mn, or no metal active sites, RNR-II (NrdJab) requiring B_{12}, and RNR-III (NrdDE) requiring two Fe atoms[45–47]. Notably, mutants in the anaerobic RNRs (Class II and III) having deficient biofilm formation[15] and impaired anaerobic growth and virulence[16]. The factors necessitating this triple redundancy in *Pseudomonas* are thought to be related to hypoxia and are not well understood.

The observation that NrdB shared a maxima with iron in both oxic and anoxic treatments of AE 500 implied this ribonucleotide reductase isoform was a major contributor to the Fe signal at this site, which is known to have 3 Fe atoms per NrdB polypeptide[48]. Interestingly, the distribution of the NrdA subunit overlapped but with a much wider distribution (SE 12-30 in oxic, Figure 7G, and SE12-35 in anoxic, Figure 7H) and had different maxima than NrdB, implying the NrdAB complex may not have been stoichiometrically assembled throughout the dimension. The alignment of NrdB with the Fe Peak in the AE 500 dimension was consistent that the divot in anoxic AE600 SE14 being an artifact of sample processing. The three most abundant iron proteins in this dimension, NrdA, NrdB, and glutamine synthetase, all show adjacent points that imply higher protein abundance if extrapolated between them (e.g. between SE13 and SE15). When linearly extrapolated these three proteins would be the major proteins with maxima close to or potentially on the Fe Peak 3 site (SE 14), implying their contribution to the iron demand here.

The increased contribution of ribonucleotide reductase to Fe Peak 3 was also consistent with the global proteome results (Figures 1 and 8). In our global experiment, the NrdAB is the dominant ribonucleotide reductase under oxic conditions, as expected from prior studies[26]. Under aerobic conditions Class I NrdAB proteins were most abundant, with less of the class II NrdJab, and no observed class III NrdD. Under anaerobic conditions all three classes of RNR's were present and in higher abundance than in oxic treatments. Similar to CobN, these results also conflict with the model proposed by Crespo et al. (2018), where a cascade of expression from NrdA to NrdJ to NrdG was expected to coincide with decreasing B_{12} availability. Together these results demonstrate a greater role for RNR under anaerobic conditions in *P. aeruginosa* and suggests this enzyme or its cofactors (Fe or B_{12}), could be potential antimicrobial targets.

Fe Peak 3d: A third ferritin annotated as "probably bacterioferritin" (PA4880) was present in the anoxic treatment adjacent to this location with a maximum at SE 18 in the AE 600 dimension (Figure 7D). The ferritins are discussed in greater detail below.

Fe Peak 4

Although a relatively minor peak compared to Fe Peaks 1 and 2, the fourth largest peak within the *P. aeruginosa* metalloproteome contained key components of the denitrification apparatus. This peak was found in the AE 200 dimension, at SE-20 and SE-22 in oxic and anoxic treatments, respectively (Table 1, Figures 2 and 3). Similar to Peak 3, the peak was much more pronounced in the anoxic treatment compared to the oxic peak with 7.0 times more Fe in the anoxic at their respective maximum locations (Figures 9G, H). This was large Fe difference occurred despite the anoxic treatment having only 9.2% more total protein (Table S1). Yet Fe Peak 4 was still the smallest of the four iron peaks, with Fe Peak 1 being 5.5 larger in the anoxic treatment. Fe Peak 4 in the oxic treatment was particularly minor, approaching background sounding baseline levels, consistent with minimal need for denitrification apparatus under oxic conditions. Notably, the Fe Peak 4 is quite broad and the known iron metalloproteins within it range from SE 18 to SE 32 (Figures 9B, D, F, and H). The denitrification system is known to be a membrane localized protein complex. Despite the high abundance of some of these proteins, the iron peak was smaller than the other three Fe peaks as mentioned above. This may be a result of underrecovery of the denitrification membrane proteins in the native, non-detergent, system.

Proteins in the Anoxic Treatment: A total of 148 proteins were detected at the anoxic maximum of Fe Peak 4, of those 18 proteins shared a maximum at that location (AE 200 SE-22, Table S3). Of those 18, NirN (PA0509) was the only known iron metalloprotein present and 11 of those were annotated as hypothetical proteins (Figures 9B, D, F). Among the remaining proteins detected at SE-22 (not just having a maxima), 9 were known iron proteins, including components of the denitrification system (Figures 9B, D, F).

Proteins in the Oxic Treatment: 162 proteins were detected at the oxic maximum of Fe Peak 4, with 27 sharing a maximum at that location (AE 200 SE-20, Table S3). Of those 27 proteins with a shared maxima none were known iron proteins and 14 were annotated as hypothetical proteins. Among the proteins detected at SE-20 (Figure 9A, C, E), four were known iron proteins, all of which were also on the list of iron proteins detected in the anoxic peak (Table S3), including nitrite reductase precursor (PA0519), cytochrome c4 precursor (PA5490), probable iron-binding protein IscU (PA3813), and cytochrome c551 peroxidase precursor (PA4587).

Fe Peak 4a-c : Under anoxic and added nitrate media conditions *Pseudomonas* utilizes denitrification-based respiration. A number of iron proteins are enlisted including NirS (4a: PA0519 nitrite reductase precursor), NapA (4b: periplasmic nitrate reductase protein NapA PA1174), and NirN (4c: PA0509). NirN is a NirS homologue, and forms a 8 blade β-propeller with a cytochrome c domain[49].

Nitrite reductase (NirS, PA0519) was highly abundant in the anoxic treatment. With reaching 475 spectral counts at its maximum, it was the 2nd most protein in the metalloproteomic dataset. While its peak is somewhat offset from the Fe/Cu peak by two SE fractions it still was at 250 spectral counts on the Fe maximum (Figures 9B, J, I).

Azurin Cu protein: The copper containing azurin enzyme (PA4922) is an electron donor to nitrite reductase (NirS)[50], and the residues involved in their protein-protein interaction have been identified characterized[51]. Here we observed the Cu peak in the AE 200 dimension to co-elute with Fe Peak 4 in both oxic and anoxic treatments (Figures 9I, J). This protein was also one of the most abundant proteins in the anoxic metalloproteome. While it was present with 30 spectral counts at the maximum in AE 200, it was highly abundant in AE 100 reaching 449 spectral counts at 100-22, where few other proteins elute.

Fe Peak 4d: IscU is an Fe-S cluster assembly scaffold, and part of the ISC (Iron Sulfur Cluster) biosynthetic system.[52] It's iron signal may be due to the presence of Fe-S within the protein scaffold. Unlike *E. coli* which has the SUF and ISC Fe-S biosynthesis systems, *P. aeruginosa* only has the ISC system and is essential for viable *Pseudomonas*, has been proposed as a target for antibiotic treatment, although the mitochondria use a homolog of the system that could be sensitive to treatments.

Fe Peak 4e: Corresponding to the occurrence of five cytochromes in this area (see below), a heme-transport protein, PhuT, (PA4708) also co-eluted, consistent with the need to assemble the prosthetic groups into the cytochromes. PhuS in *P. aeruginosa* has been shown to contribute heme to heme oxygenase and to in sensing and maintaining iron homeostasis.[53] PhuT may have a role in contributing to denitrification cytochromes.

Fe Peak 4f-j: Five cytochrome proteins were observed in this range, including cytochrome c4 precursor, cytochrome c-551 precursor, cytochrome c551 peroxidase precursor, cytochrome c5, and cytochrome c-type protein NapB precursor (PA5490, PA0518, PA4587, PA5300, PA1173). Cytochrome proteins help to conduct electrons, they contain the prosthetic group heme, which coordinates an Fe atom at its center. The co-elution of these five cytochromes at the Fe Peak 4 was consistent with their involvement in the denitrification system, and a cytochrome from *Thermus thermophilus* has been proposed to be part of a super complex with nitrate reductase[54].

Fe Peak 4 - Non-Fe metalloproteins: In addition to azurin two additional non-iron metalloproteins were detected at Fe Peak 4, nitrous-oxide reductase precursor (PA3392, Cu, anoxic only), probable glutathione peroxidase (PA0838, Se, oxic and anoxic).

Iron Storage Proteins – Bacterioferritin and Ferritin

Given the importance of iron for the variety of metalloenzymes and biochemical functions described above, the ability to store iron when excess is available and to prevent intracellular toxicity is important for bacterial cells. Ferritins are proteins whose 24 subunits combine to form a protein sphere that stores ~4000 iron atoms within as iron oxide. Bacterioferritins are bacterial versions of ferritin that also differ Eukaryotic ferritins in containing heme between subunits[55]. In a prior application of metalloproteomics on the bacterium *Pseudoalteromonas*, iron storage within two copies of bacterioferritin was identified as the major reservoir of iron within that microbes[19]. Within *P. aeruginosa's* genome (PAO1) there are three annotated ferritin genes, a bacterioferritin (BfrB, PA3531), a "bacterial ferritin" (FtnA, PA4235), and a probable bacterioferritin (PA4880). There is also a bacterioferritin comigratory protein in the PAO1 genome (PA1008).

Prior structural analysis revealed that *P. aeruginosa* BfrB coordinates heme iron between subunits, while FtnA does not[56], and that a knockout BfrB *P. aeruginosa* strain did not accumulate iron within another ferritin molecule, leading to their conclusion that BfrB (PA3531) was the main iron storage molecule[57]. Moreover, the *P. aeruginosa* FtnA (PA4235) protein was described as a ferritin distinct from bacterioferritin[58] that assembles as a heterooligomer 24mer from both BfrB and FtnA subunits. A decreasing ratio of BfrB to FtnA was observed at low oxygen, with FtnA becoming the dominant subunit under low oxygen conditions reaching ~30% to 70%[56].

While these first two ferritins (PA3531 and PA4235) have been previously studied, less work has been done on the 2nd bacterioferritin (and third ferritin overall), PA4880. Recent structural studies by Rajapaksha et al[59] showed that PA4880 adopts a 12-mer structure similar to Dps proteins, but lacks the iron coordinating ligands of Dps. Rajapaksha et al. named this gene DpsL (for Dps-like) and suggested that this protein may contribute to avoiding iron toxicity and as well as "innate immune mechanisms consisting of restriction endonucleases and cognate methyl transferases."

The current metalloproteome study provides a whole organism assessment of the iron storage capabilities in *P. aeruginosa*. Since both the global and metalloproteomic techniques used here measure tryptic peptides, we verified that these three ferritins do not share any tryptic peptides that could cause misidentification from their peptidic constituents (see Figure S4-S6 for sequence alignments). In our metalloproteomes, PA3531 (BfrB) and PA4235 (FtnA) both co-elute with in Fe Peak 1 and PA4880 (DpsL) elutes in Fe Peak 3 (Figure 10). The bacterioferritin-associated ferredoxin Bfd (PA3530) was not identified in either the anoxic or oxic metalloproteome.

The hypothesis that the contribution of ferritin (PA4235) increases under anoxic conditions by Yao et al.[56] was supported by our percentage contribution results: PA4235 was the only one of the three proteins to increase in percent contribution across the treatments from 8.2% to 22.2% between oxic and anoxic experiments (Table S1). There also appeared to be support for the accompanying hypothesis that BfrB and FtnA combine as heterogenous subunits to form a single ferritin 24mer protein complex[56]. We observed the ratio of BfrB:Ftn (PA4235:PA3531) to be highest in the AE 400 anoxic treatment with ratios of 1.1 and 7 between fractions 17 and 25 where many of these ferritins eluted (Figure 10).

Notably the contribution to the native proteome in terms of total spectral counts showed PA4880 to be the most abundant with 76.5% of spectral counts in the oxic treatment and 60.9% in the anoxic treatment (Table S1), implying PA4880 was the most abundant ferritin within *Pseudomonas aeruginosa* under these conditions. PA4880 was the dominant ferritin in AE 500 and AE 600 and coincided with the iron distributions, at SE 17 (oxic) and 18 (anoxic) for AE 500 (Figure 10). Notably, PA4880 was not present in oxic AE 600, while it showed a large peak at SE 26 in anoxic AE 600, implying increased use of this bacterioferritin under anoxic conditions. This prevalence of PA4880 also contrasts with Eshelman et al. (2017) report of PA3531 as the dominant iron store in *P. aeruginosa*. Our approach assumes that the ionization efficiency of tryptic peptide constituents across these three proteins is largely averaged out, and that there are similar number of peptides based on their similar small size. More accurate assessments could be conducted in the future by use of targeted proteomics methods[60].

In terms of the amount of iron stored within each of the three ferritins, the metalloproteomic approach could assess this. Yet the high complexity of the *P. aeruginosa* iron metalloproteome makes this less straightforward compared to the straightforward approach used in our prior study on the simpler marine bacterium *Pseudoalteromonas*[19]. From the metalloproteomic data and media conditions of this study, it appears that the extent that the Fe metallome was stored varied considerably between oxic and anoxic treatments. In oxic treatment the two Fe Peak 1 ferritins BfrB and FtnA (PA3531 and PA4235) co-eluted with the major iron peak (Figures 4 and 10), whereas under anoxic conditions they were offset by one higher SE contributing to the shoulder. The extent of iron stored within these three ferritin proteins does not appear to dominate the iron metallome as it did in *Pseudoalteromonas*[19], being a relatively minor peaks compared to the iron metalloproteins, which are offset from the iron maxima, even with the high stoichiometry when fully loaded (~4000 atoms/24 mer complex).

Detection of Iron Supercomplexes

The native metalloproteomic method used in this study purposefully does not use detergents in order to maintain metal-protein interactions. An additional advantage to omitting the use of detergents is that protein complexes can remain intact within the 2D chromatographic separations. As a result, the elution of proteins in native 2D space would not be expected to follow the size and charge state of the protein monomers, but instead will reflect those of multimers and protein complexes. An indication of this is shown in Figure 10, where the distribution of molecular weights with size exclusion in each anion exchange fraction follows a downward trend, but also includes many proteins that do not follow this trend, eluting at sizes higher than their monomer molecular weight.

Here the four major Fe peaks identified in our study also appear to be related to protein complexes present in the cytosol of *P. aeruginosa*. In particular, the co-elution of proteins with related functions and co-located with dedicated iron storage systems implies a level of cellular organization at the protein-protein interaction level that is optimized for prioritization of metal distribution and trafficking. The presence of protein supercomplexes, assembles of multiple enzymes complexes (complexes of complexes) has been observed by native gel and chromatographic methods. For example the respiratory complexes, termed respirasomes, within mitochondria and bacteria contain assemblies of respiratory chain complexes III and IV, each containing one or more enzymes[61,62]. The potential ability to observe and study supercomplexes from the entire soluble proteome and to observe their association with iron homeostasis is exciting. Application of recent AI-based structural modeling to examining protein-protein interactions[23] allowed exploration of the potential for protein complexes among co-eluting proteins not typically thought to form complexes. For example, a trimer protein complex was modeled with constituents of Fe Peaks 1 and 2 (PA2009, PA1787 and PA4022; Figure 11). The co-elution of this suite of proteins, including (bacterio)ferritins of largely different molecular weights implies cellular organization combining the role of key metabolic functions with the supply and biosynthesis of iron and its prosthetic groups within *Pseudomonas*. Co-locating multiple abundant and metabolically important iron enzymes with ferritins molecules would be advantageous, contributing to both the metalation and the prioritization of those metabolisms. Future studies could confirm these presence of these iron supercomplexes and interrogate the regulation and structural biology behind them. While originally conceived as a methodology capable of investigating metalloproteins, this native 2D approach also serves to contribute information about protein-protein interactions that pertain to cellular metal homeostasis.

Data Availability

The metalloproteomic metal and protein data have been submitted to Zenodo. The code for this project is available at https://github.com/maksaito/Metalloproteomic-Viewer (Version 11)

Acknowledgements

We thank Dawn Moran for microbiological isolations and Viktoria Steck for assistance with genome sequencing samples. We thank Kevin Waldron for helpful discussions. The research was supported by NIH R01GM135709, the Simons Foundation, and the Center for Chemical Currencies on a Microbial Planet (contribution #069), and NSF projects 2123055, 2125063, 2048774.

References

1. N. J. Palleroni, *Microbiology*, 2003, **149**, 1–7.
2. N. Palleroni and I. Genius, *Bergey's manual of systematic bacteriology*, 1984, **1**, 141–199.
3. G. P. Bodey, R. Bolivar, V. Fainstein and L. Jadeja, *Reviews of Infectious Diseases*, 1983, **5**, 279--313.
4. E. Tacconelli, E. Carrara, A. Savoldi, S. Harbarth, M. Mendelson, D. L. Monnet and et al., *The Lancet Infectious Diseases*, 2018, **18**, 318--327.
5. E. P. Skaar and M. Raffatellu, *Metallomics*, 2015, **7**, 926–928.
6. N. Kimata, T. Nishino, S. Suzuki and K. Kogure, *Microb Ecol*, 2004, **47**, 41–47.
7. S. Crone, M. Vives-Flórez, L. Kvich, A. M. Saunders, M. Malone, M. H. Nicolaisen, E. Martínez-García, C. Rojas-Acosta, M. Catalina Gomez-Puerto, H. Calum, M. Whiteley, R. Kolter and T. Bjarnsholt, *APMIS*, 2020, **128**, 220–231.
8. B. Borer, I. H. Zhang, A. E. Baker, G. A. O'Toole and A. R. Babbin, *PNAS Nexus*, 2023, **2**, pgac311.
9. C. A. Carlson and J. L. Ingraham, *Applied and Environmental Microbiology*, 1983, **45**, 1247--1253.
10. K. L. Thomas, D. Lloyd and L. Boddy, *FEMS Microbiology Letters*, 1994, **118**, 181--186.
11. A. J. Jesaitis, M. J. Franklin, D. Berglund, M. Sasaki, C. I. Lord, J. B. Bleazard, J. E. Duffy, H. Beyenal and Z. Lewandowski, *The Journal of Immunology*, 2003, **171**, 4329--4339.
12. B. E. Poulsen, R. Yang, A. E. Clatworthy, T. White, S. J. Osmulski, L. Li, C. Penaranda, E. S. Lander, N. Shoresh and D. T. Hung, *Proc Natl Acad Sci U S A*, 2019, **116**, 10072–10080.
13. C. Stover, X. Pham, A. Erwin, S. Mizoguchi, P. Warrener, M. Hickey, F. Brinkman, W. Hufnagle, D. Kowalik and M. Lagrou, *Nature*, 2000, **406**, 959–964.
14. I. J. Schalk and Q. Perraud, *Environmental Microbiology*, 2023, **25**, 811–831.
15. M. C. Mastropasqua, M. D'Orazio, M. Cerasi, F. Pacello, A. Gismondi, A. Canini, L. Canuti, A. Consalvo, D. Ciavardelli, B. Chirullo and P. Pasquali, *Molecular Microbiology*, 2017, **106**, 543--561.
16. M. M. Golden, A. C. Heppe, C. L. Zaremba and W. Wuest, *RSC Chemical Biology*, DOI:10.1039/D4CB00175C.
17. J. P. Barnett, D. J. Scanlan and C. A. Blindauer, *Anal Bioanal Chem*, 2012, **402**, 3371–3377.
18. A. Cvetkovic, A. L. Menon, M. P. Thorgersen, J. W. Scott, F. L. Poole II, F. E. Jenney Jr, W. A. Lancaster, J. L. Praissman, S. Shanmukh and B. J. Vaccaro, *Nature*, 2010, **466**, 779–782.
19. M. G. Mazzotta, M. R. McIlvin and M. A. Saito, *Metallomics*, 2020, **12**, 654–667.
20. M. G. Mazzotta, M. R. McIlvin, D. M. Moran, D. T. Wang, K. D. Bidle, C. H. Lamborg and M. A. Saito, *Metallomics*, 2021, **13**, mfab060.
21. J. K. Saunders, M. R. McIlvin, C. L. Dupont, D. Kaul, D. M. Moran, T. Horner, S. M. Laperriere, E. A. Webb, T. Bosak and A. E. Santoro, *Proceedings of the National Academy of Sciences*, 2022, **119**, e2200014119.
22. N. R. Cohen, M. R. McIlvin, D. M. Moran, N. A. Held, J. K. Saunders, N. J. Hawco, M. Brosnahan, G. R. DiTullio, C. Lamborg and J. P. McCrow, *Nature Microbiology*, 2021, **6**, 173–186.
23. J. Abramson, J. Adler, J. Dunger, R. Evans, T. Green, A. Pritzel, O. Ronneberger, L. Willmore, A. J. Ballard and J. Bambrick, *Nature*, 2024, 1–3.

24 D. A. Rodionov, A. G. Vitreschak, A. A. Mironov and M. S. Gelfand, *Journal of Biological Chemistry*, 2003, **278**, 41148–41159.
25 G. M. Teitzel, A. Geddie, S. K. De Long, M. J. Kirisits, M. Whiteley and M. R. Parsek, *Journal of bacteriology*, 2006, **188**, 7242–7256.
26 A. Crespo, N. Blanco-Cabra and E. Torrents, *Frontiers in Microbiology*, 2018, **9**, 986.
27 J. M. Dunwell, A. Purvis and S. Khuri, *Phytochemistry*, 2004, **65**, 7–17.
28 C. J. Harmer, M. Wynn, R. Pinto, S. Cordwell, B. R. Rose, C. Harbour, J. A. Triccas and J. Manos, *PLoS One*, 2015, **10**, e0134229.
29 D. B. Ascher, O. Spiga, M. Sekelska, D. E. V. Pires, A. Bernini, M. Tiezzi, J. Kralovicova, I. Borovska, A. Soltysova, B. Olsson, S. Galderisi, V. Cicaloni, L. Ranganath, A. Santucci and A. Zatkova, *Eur J Hum Genet*, 2019, **27**, 888–902.
30 D. J. Hassett, M. D. Sutton, M. J. Schurr, A. B. Herr, C. C. Caldwell and J. O. Matu, *Trends in microbiology*, 2009, **17**, 130–138.
31 K. Taniyama, H. Itoh, A. Takuwa, Y. Sasaki, S. Yajima, M. Toyofuku, N. Nomura and N. Takaya, *Journal of bacteriology*, 2012, **194**, 1447–1456.
32 L. Castro, V. Tórtora, S. Mansilla and R. Radi, *Accounts of chemical research*, 2019, **52**, 2609–2619.
33 D. J. Hassett, W. A. Woodruff, D. J. Wozniak, M. L. Vasil, M. S. Cohen and D. E. Ohman, *J Bacteriol*, 1993, **175**, 7658–7665.
34 B. Polack, D. Dacheux, I. Delic-Attree, B. Toussaint and P. M. Vignais, *Infect Immun*, 1996, **64**, 2216–2219.
35 J. K. Saunders, D. A. Gaylord, N. A. Held, N. Symmonds, C. L. Dupont, A. Shepherd, D. B. Kinkade and M. A. Saito, *Journal of proteome research*, 2020, **19**, 4718–4729.
36 L. Chen, Q. W. Xie and C. Nathan, *Mol Cell*, 1998, **1**, 795–805.
37 L. C. Seaver and J. A. Imlay, *Journal of bacteriology*, 2001, **183**, 7173–7181.
38 N. J. Hare, N. E. Scott, E. H. H. Shin, A. M. Connolly, M. R. Larsen, G. Palmisano and S. J. Cordwell, *Proteomics*, 2011, **11**, 3056–3069.
39 J. T. Lee, S. S. Lee, S. Mondal, B. N. Tripathi, S. Kim, K. W. Lee, S. H. Hong, H.-W. Bai, J.-Y. Cho and B. Y. Chung, *Mol Cells*, 2016, **39**, 594–602.
40 K. Nishida-Tamehiro, A. Kimura, T. Tsubata, S. Takahashi and H. Suzuki, *Plos one*, 2022, **17**, e0272090.
41 T. Yagi, *Journal of bioenergetics and biomembranes*, 1991, **23**, 211–225.
42 A. L. Pey, C. F. Megarity and D. J. Timson, *Bioscience Reports*, 2019, **39**, BSR20180459–BSR20180459.
43 K. Brown-Grant and J. Tata, *The Journal of Physiology*, 1961, **157**, 157.
44 I. Borovok, B. Gorovitz, M. Yanku, R. Schreiber, B. Gust, K. Chater, Y. Aharonowitz and G. Cohen, *Molecular Microbiology*, 2004, **54**, 1022--1035.
45 A. Jordan, E. Torrents, I. Sala, U. Hellman, I. Gibert and P. J. Reichard, *Journal of Bacteriology*, 1999, **181**, 3974--3980.
46 E. J. Blaesi, G. M. Palowitch, K. Hu, A. J. Kim, H. R. Rose, R. Alapati, M. G. Lougee, H. J. Kim, A. T. Taguchi and K. O. Tan, *Proceedings of the National Academy of Sciences*, 2018, **115**, 10022--10027.
47 J. Stubbe and M. R. Seyedsayamdost, *ACS Publications*.
48 E. Torrents, M. Westman, M. Sahlin and B.-M. Sjoberg, *Journal of Biological Chemistry*, 2006, **281**, 25287–25296.
49 T. Klünemann, A. Preuß, J. Adamczack, L. F. M. Rosa, F. Harnisch, G. Layer and W. Blankenfeldt, *J Mol Biol*, 2019, **431**, 3246–3260.
50 T. Kakutani, H. Watanabe, K. Arima and T. Beppu, *J Biochem*, 1981, **89**, 463–472.

51 M. Kukimoto, M. Nishiyama, M. Tanokura, E. T. Adman and S. Horinouchi, *J Biol Chem*, 1996, **271**, 13680–13683.

52 A. Romsang, J. M. Dubbs and S. Mongkolsuk, *Stress and Environmental Regulation of Gene Expression and Adaptation in Bacteria*, 2016, 1090–1102.

53 A. P. Kaur, I. B. Lansky and A. Wilks, *Journal of Biological Chemistry*, 2009, **284**, 56–66.

54 F. Cava, O. Zafra and J. Berenguer, *Molecular microbiology*, 2008, **70**, 507–518.

55 M. J. Grossman, S. M. Hinton, V. Minak-Bernero, C. Slaughter and E. I. Stiefel, *Proc Natl Acad Sci U S A*, 1992, **89**, 2419–2423.

56 H. Yao, A. Soldano, L. Fontenot, F. Donnarumma, S. Lovell, J. R. Chandler and M. Rivera, *Biomolecules*, 2022, **12**, 366.

57 K. Eshelman, H. Yao, A. N. D. Punchi Hewage, J. J. Deay, J. R. Chandler and M. Rivera, *Metallomics*, 2017, **9**, 646–659.

58 H. Yao, G. Jepkorir, S. Lovell, P. V. Nama, S. Weeratunga, K. P. Battaile and M. Rivera, *Biochemistry*, 2011, **50**, 5236–5248.

59 N. Rajapaksha, H. Yao, A. Cook, S. Seibold, L. Liu, K. P. Battaile, L. Fontenot, F. Donnarumma, S. Lovell and M. Rivera, *Front Mol Biosci*, 2024, **11**, 1390745.

60 M. A. Saito, M. R. McIlvin, D. M. Moran, A. E. Santoro, C. L. Dupont, P. A. Rafter, J. K. Saunders, D. Kaul, C. H. Lamborg and M. Westley, *Nature Geoscience*, 2020, **13**, 355–362.

61 R. Vartak, C. A.-M. Porras and Y. Bai, *Protein & cell*, 2013, **4**, 582–590.

62 A. Stroh, O. Anderka, K. Pfeiffer, T. Yagi, M. Finel, B. Ludwig and H. Schägger, *Journal of biological chemistry*, 2004, **279**, 5000–5007.

Table 1. Major Fe peaks in the oxic and anoxic metalloproteome of *Pseudomonas aeruginosa*.

Peak Number and Rank	Location Oxic (AE-SE)	Fe value Oxic (ppb)	Location Anoxic (AE-SE)	Fe value Anoxic (ppb)	Biochemical Function(s)
1	400-14	40.5	400-15	158.96	Respiration
2	300-17	25.7	300-18	46.2	Oxidative Stress
3	600-18	11.6	600-14	57.8	DNA production
4	200-20	4.1	200-22	28.7	Denitrification

Figure Captions

Figure 1. Global proteomic abundance data for selected metabolic and metal related systems in *P. aeruginosa* grown under aerobic and anaerobic conditions, where yellow is more abundant (values normalized to the sum of spectral counts for the two treatments; extraction triplicates were averaged). Strong responses were observed in nitrogen, iron, molybdenum and cobalt related systems. These global proteomes are sample splits of those used for the metalloproteomic dataset in this study.

Figure 2. The Fe metalloproteome of *P. aeruginosa* under oxic (left) and anoxic (right) conditions in 3D and 2D views reveals four major iron peaks (numbered, Table 1). The peaks were associated with major cellular processes, 1) oxic respiration, 2) ROS detoxification, with 3) RNA production, and 4) denitrification. AE refers to the first dimension of anion exchange. SE refers to the second dimension of size exclusion. Iron (Fe 56) is in units of ppb.

Figure 3. The iron metallome in 2D native space under oxic and anoxic conditions, and compared with the following iron metalloproteins: aconitate hydratase 2 (PA1787), homogentisate 1,2-dioxygenase (PA2009), hydrazone dehydrogenase HdhA (PA4022), bacterial ferritin (PA4235), and bacterioferritin (PA3531). Notably some of these iron proteins have broad peaks (PA1787, PA4022) or double peaks (PA2009, PA4235) that extend beyond the iron maximum region, which may be due to apo (unmetalled) or partially metalated isoforms.

Figure 4. Iron proteins that contribute to Fe Peak 1, examined in 1D along the size exclusion fractions derived from the 400 AE dimension. The iron maxima in this dimension aligns with the peak maxima of homogentisate 1,2-dioxygenase (PA2009) in both oxic and anoxic conditions, while the much larger aconitate hydratase 2 (PA1787) peak is offset by slightly offset by two SE fractions under both conditions, however this protein has a large broad distribution in native space (see Figure 2). The iron enzyme hydrazone dehydrogenase HdhA (PA4022) also co-eluted with Peak 1, and transitions from being a minor peak in the oxic conditions to a major peak in the anoxic conditions. The ferritins (PA3531 and PA4235) align with the iron maxima under oxic conditions but are also slightly offset by SE 1 fraction under anoxic conditions. The iron peak has a shoulder in the 16-21 SE fraction range, in both oxic and anoxic conditions from the confluence of these metalloprotein peaks.

Figure 5. Optimization contributions of proteins to Fe peak 1 under oxic and anoxic conditions. Note that PA2009 has a second peak at SE 23 under oxic conditions (see Figure 4) that may be an apo form. Because there is no iron peak at that location, the optimization results in a 0% contribution (Original). When the second peak of PA2009 was removed (top left panel), PA2009 contributes 45.7% of the Peak 1 area and PA4022 goes to 0%. In the anoxic treatment the optimization produces a 0.0% contribution of PA1787, which similarly may be due to the broad and potentially apo forms of this abundant enzyme. In the embedded table percent contributions to each optimization and the optimized coefficients (*100 for readability) are shown.

Figure 6. Iron proteins that contribute to Fe Peak 2, examined in 1D along the size exclusion fractions derived from the 300 AE dimension. The iron maxima in this dimension aligns with the peak maxima of superoxide disumutase (PA4366) in both oxic and anoxic conditions. Aconitate hydratase 2 (PA1787) is observed in Fe Peak 2, and it also observed in Fe Peak 1 (Figures 3, 4). As in Peak 1, it was also offset by 1-2 SE fractions under both conditions and has a large broad distribution in native space (see Figure 2). Two copies of the iron enzyme alkylhydroperoxide (PA3529 and PA0139) co-eluted with Peak 2, with

PA3529 going from the 3rd largest peak in oxic conditions to the largest peak in anoxic conditions, likely due to the need to address increased organic peroxides when growing on nitrate. and transitions from being a minor peak in the oxic conditions to a major peak in the anoxic conditions. Minor contributors to Fe Peak 2 included quinone oxidoreductase, a second copy of aconitate hydratase, and 3-isopropylmalate dehydratase large subunit (middle panels). There is a shoulder in Fe Peak 2 on the left side of the oxic peak at SE 15, likely contributed to by PA1787. The dotted grey line in all panels represents the local of the Fe maximum in AE 300, and the Fe anoxic peak was larger than under oxic conditions.

Figure 7. Proteins eluting at Fe Peak 3 in the AE 600 (A-F) and AE 500 (G-J) 1st dimension fractions. Dotted grey represents the iron maxima.

Figure 8. The ribonucleotide reductase enzyme complexes within oxic and anoxic treatments. NrdA/B, and NrdD/G require iron, while NrdJa/Jb requires vitamin B_{12}. Bars are the average and error bars represent standard deviation of the extraction triplicates.

Figure 9. Metalloproteins associated with Fe Peak 4 20 oxic and at anoxic treatments (panels A-F), dashed line is the location of the iron maxima under each condition (AE 200 SE and AE 200 SE 22). Element traces along AE 200 dimension for Fe, Cu, Ni, Zn, and P traces along the AE 200 dimension (panels G-P), dashed line is the maximum for each element. Left and right panels are oxic and anoxic treatments, respectively. Panels C and D are the same as A and B, but without PA0519 to allow examination of lower abundance proteins. Proteins shown are known metalloproteins detected at the iron maxima positions, see Table S3 for list of proteins.

Figure 10. Abundance and ratios of ferritin iron storage in *P. aeruginosa*. Distributions of bacterioferritin (PA3531), ferritin (PA4235), and probable bacterioferritin/Dps-like protein (DpsL; PA4880) shown in the 300-600 anion exchange (AE) fractions of the first dimension and 10-35 size exclusion (SE) fractions of the second dimension. PA3531, PA4235, and PA4880 each had highest spectral counts in AE 300, 400, and 500-600, respectively. Consistent with Yao et al., 2022, the ratio of BfrB:Ftn (PA4235:PA3531) was highest in the AE 400 anoxic treatment with ratios of 1.1 and 7 between fractions 17 and 25 where much of both ferritins eluted. (The maxima for both were slightly offset between treatments both PA3531 and PA4235) have a maximum at SE14 in oxic and SE16 in anoxic, likely due to slightly different chromatographies between experiments).

Figure 11. Molecular weight distributions relative to size exclusion in each of the size anion exchange fractions (for oxic dataset). The decreasing trend in each fraction is consistent with the larger proteins elute at lower numbers. The presence of proteins in the bottom left corner of each plot is consistent with the presence of protein complexes, where smaller proteins form complexes and elute at lower SE fractions than expected based on their size.

Figure 12. Alphafold3 model of putative protein complex consistent with their observed co-elution in native metalloproteomic analyses with PA2009, PA1787 and PA4022.

Figure 1.

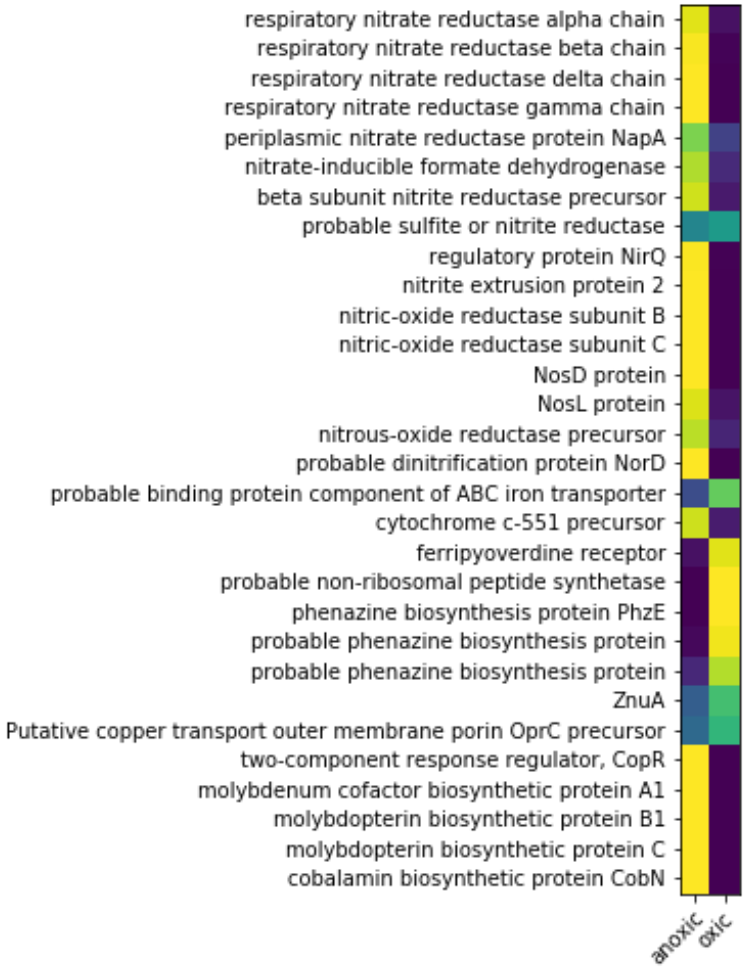

1 **Figure 2.**

2

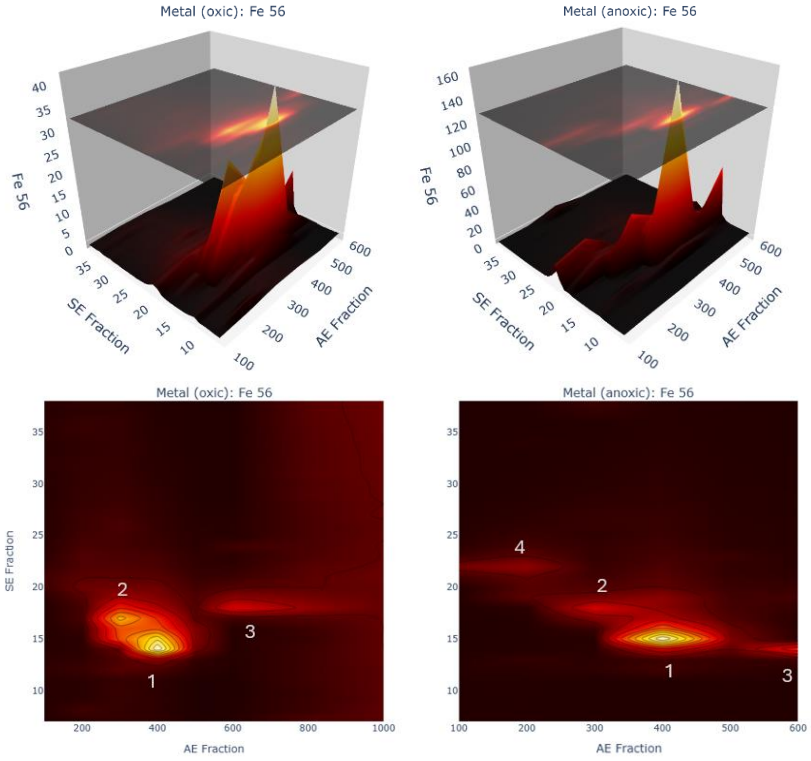

Figure 3.

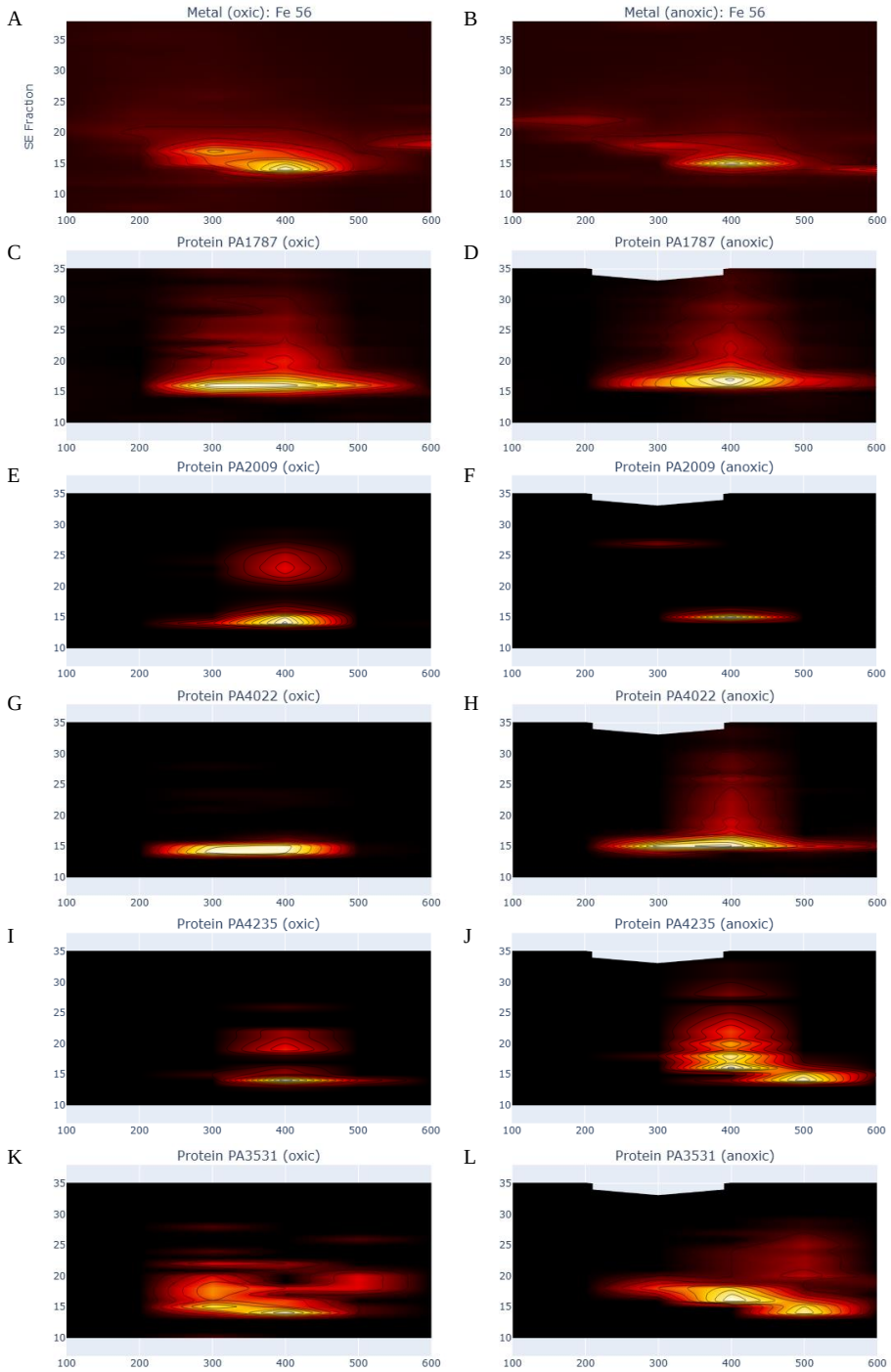

Figure 4.

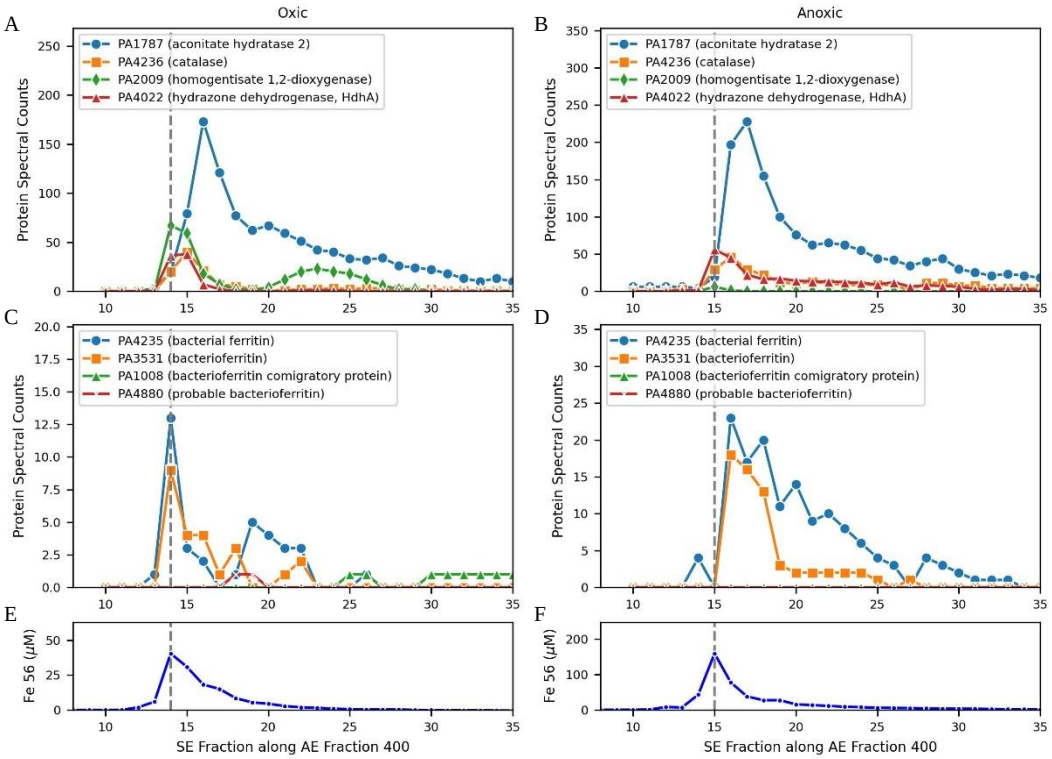

Figure 5.

A

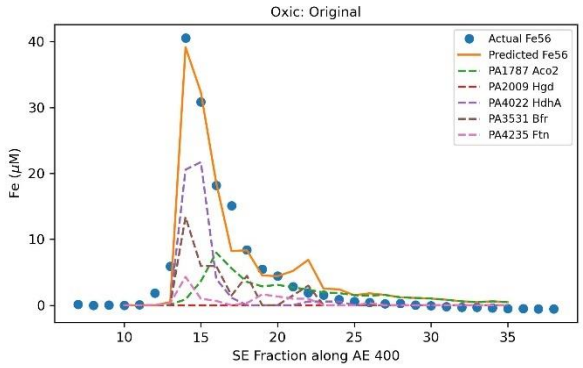

B

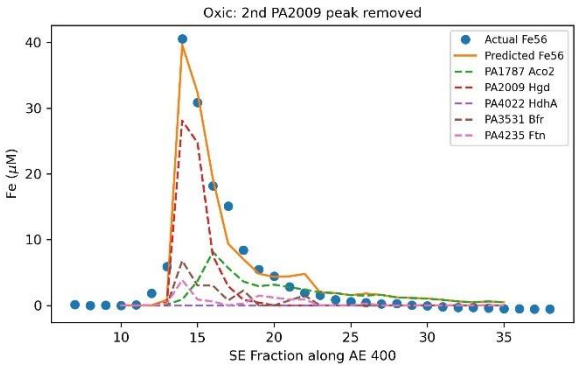

C

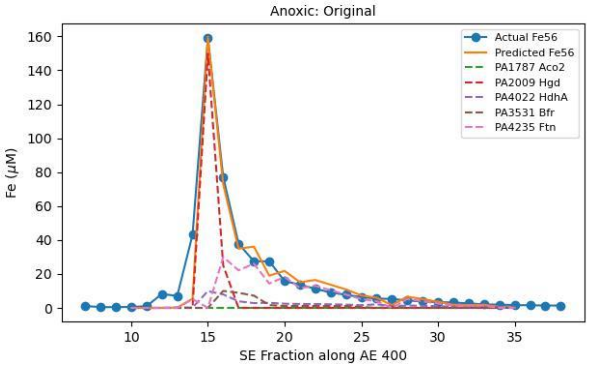

D

Protein ID	Oxic: Original	Oxic: 2nd PA2009 peak removed	Anoxic
PA1787	32.9% (4.6)	34% (4.7)	0.0% (0)
PA2009	0.00% (0)	45.7% (41.9)	39.5% (2496)
PA4022	34.1% (57)	0.00% (0)	11.2% (17.6)
PA3531	24.8% (148)	12.8% (75.5)	7.8% (55.5)
PA4235	8.3% (33)	7.5% (29.7)	41.5% (130)

Figure 6

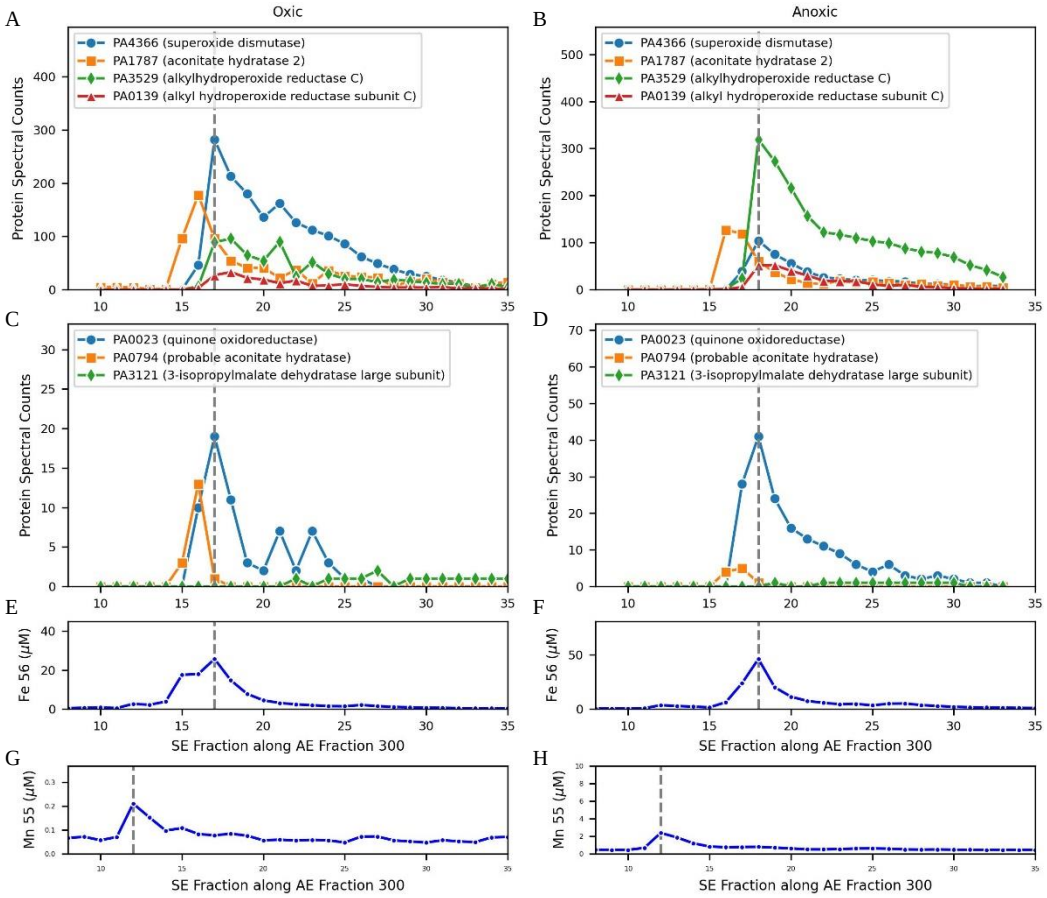

1 **Figure 7**.

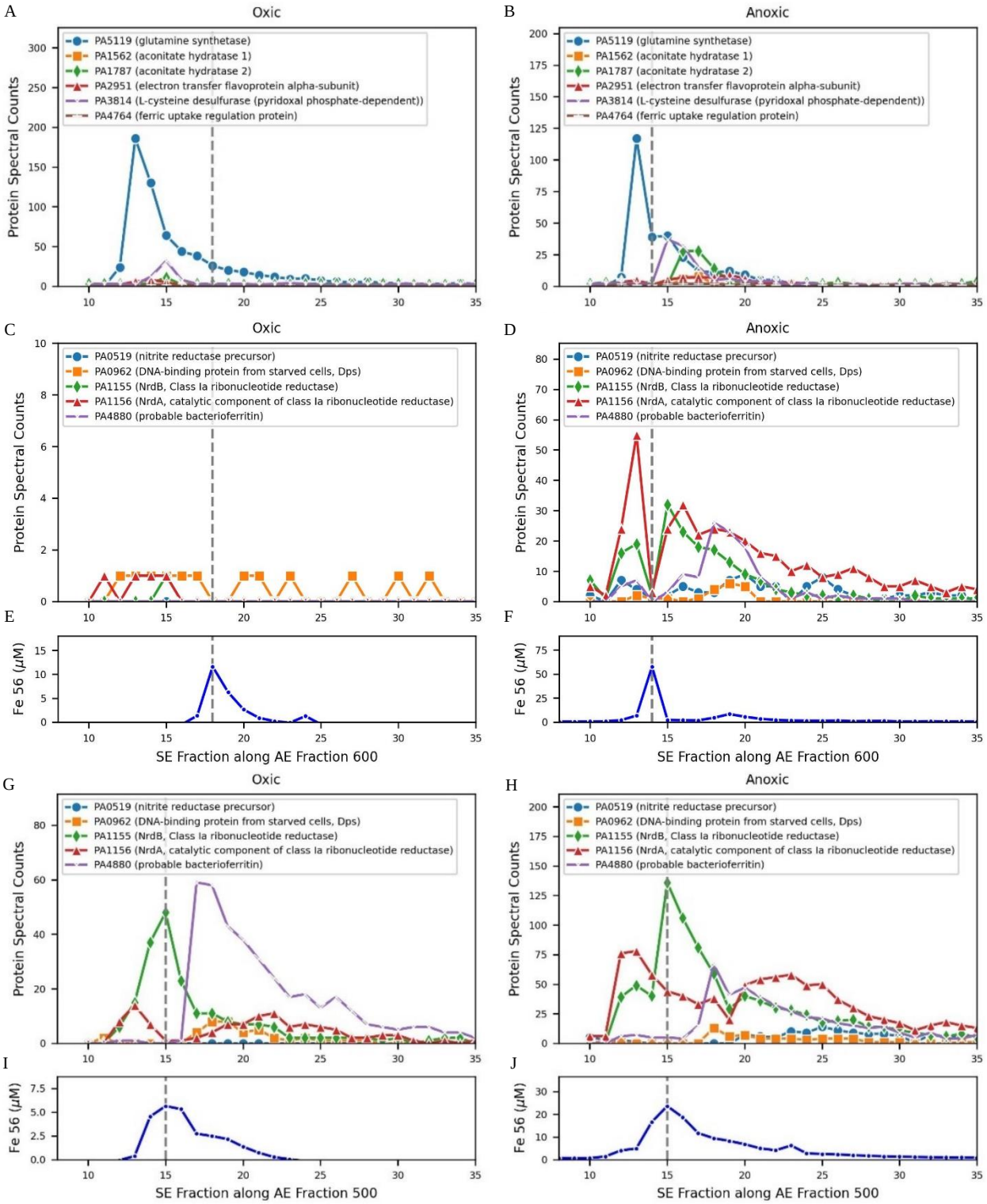

1 **Figure 8.**

2

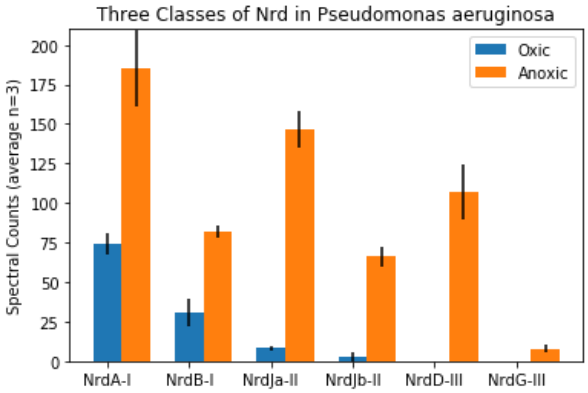

Figure 9.

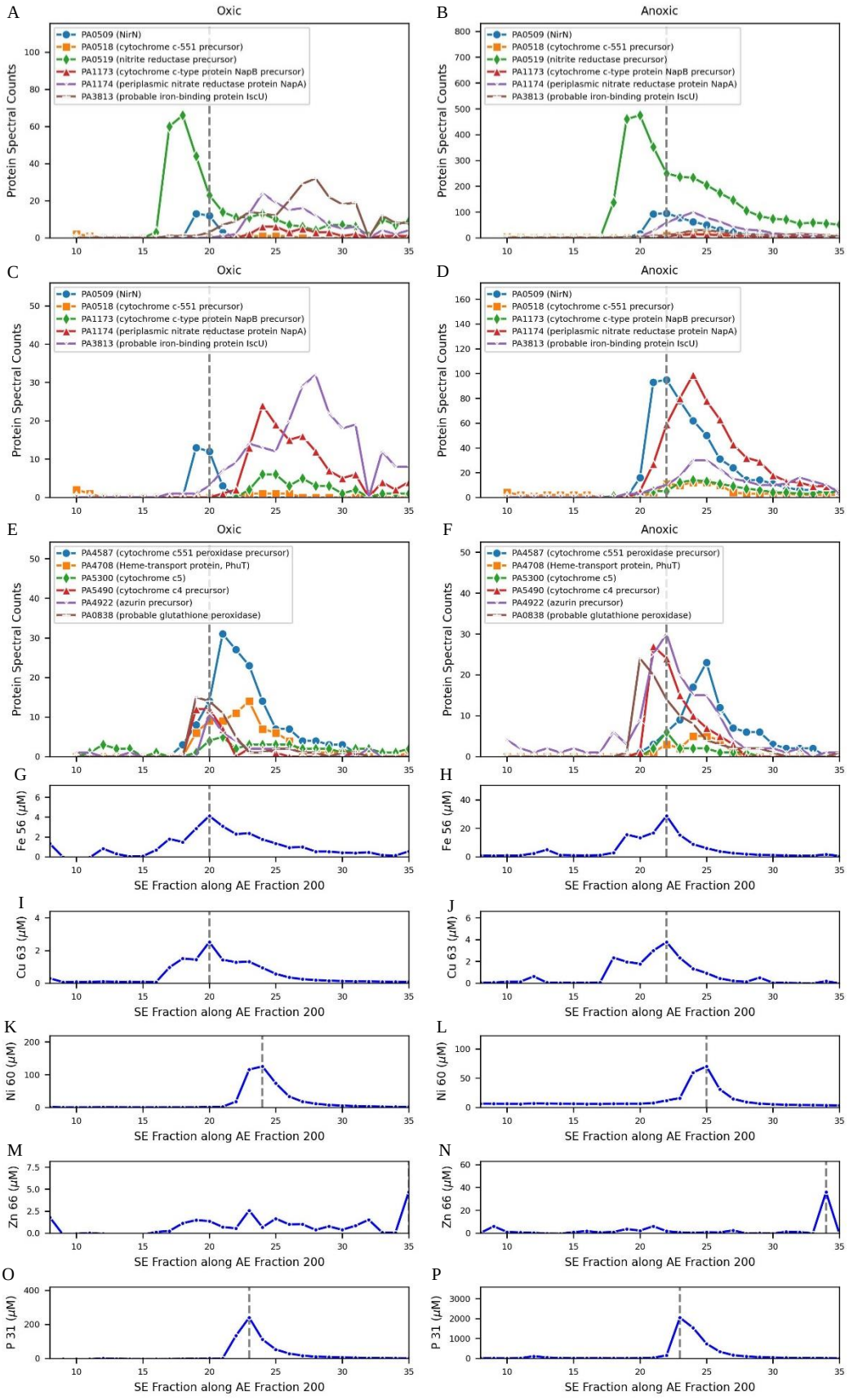

Figure 10.

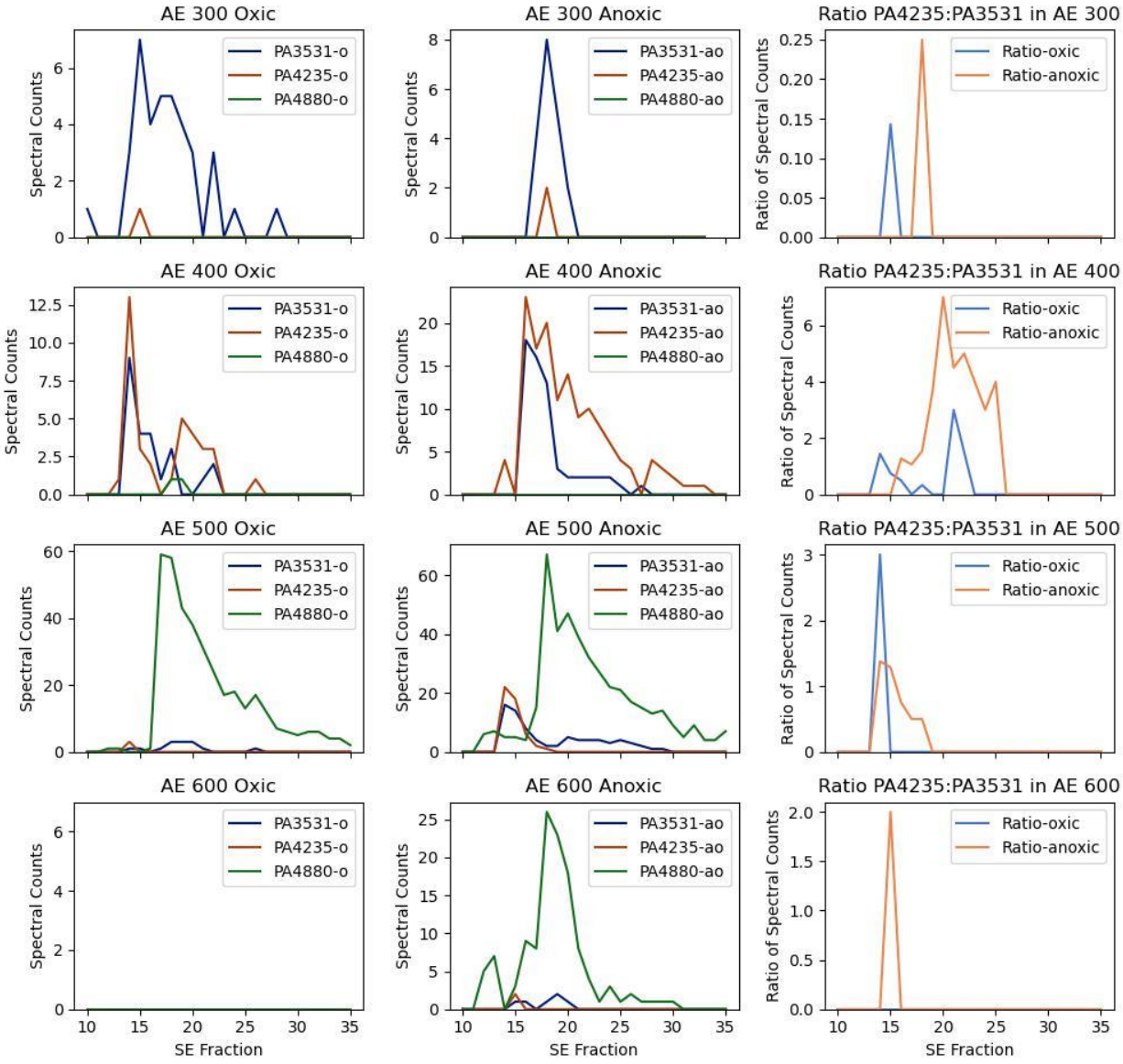

Figure 11.

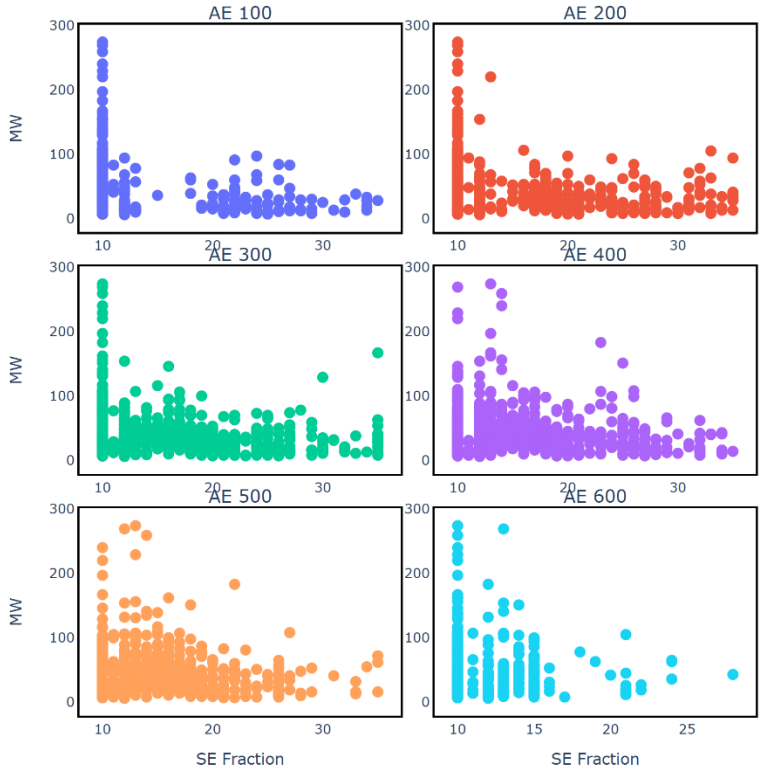

Figure 12.

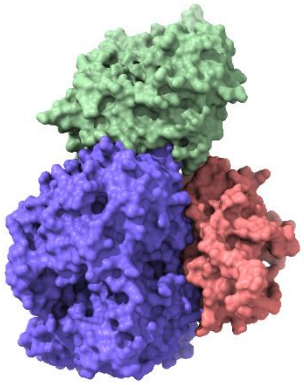

1